CrossMark

The TESS-Keck Survey. XVIII. A Sub-Neptune and Spurious Long-period Signal in the TOI-1751 System

Anmol Desai[1], Emma V. Turtelboom[1], Caleb K. Harada[1,33], Courtney D. Dressing[1], David R. Rice[2],
Joseph M. Akana Murphy[3,33], Casey L. Brinkman[4], Ashley Chontos[5,34], Ian J. M. Crossfield[6], Fei Dai[7,8,35],
Michelle L. Hill[9], Tara Fetherolf[9,10], Steven Giacalone[8,36], Andrew W. Howard[11], Daniel Huber[4,12],
Howard Isaacson[1,13], Stephen R. Kane[9], Jack Lubin[14], Mason G. MacDougall[15], Andrew W. Mayo[1,16],
Teo Močnik[17], Alex S. Polanski[6], Malena Rice[18], Paul Robertson[14], Ryan A. Rubenzahl[8,33], Judah Van Zandt[15],
Lauren M. Weiss[19], Allyson Bieryla[20], Lars A. Buchhave[21], Jon M. Jenkins[22], Veselin B. Kostov[23,24],
Alan M. Levine[25], Jorge Lillo-Box[26], M. Paegert[20], Markus Rabus[27], S. Seager[25,28,29], Keivan G. Stassun[30],
Eric B. Ting[22], David Watanabe[31], and Joshua N. Winn[32]

[1] Department of Astronomy, 501 Campbell Hall, University of California, Berkeley, CA 94720, USA; eturtelboom@berkeley.edu
[2] Astrophysics Research Center, Department of Natural Sciences, The Open University of Israel, Raanana 4353701, Israel
[3] Department of Astronomy and Astrophysics, University of California, Santa Cruz, CA 95064, USA
[4] Institute for Astronomy, University of Hawai'i, 2680 Woodlawn Drive, Honolulu, HI 96822, USA
[5] Department of Astrophysical Sciences, Princeton University, 4 Ivy Lane, Princeton, NJ 08540, USA
[6] Department of Physics and Astronomy, University of Kansas, Lawrence, KS, USA
[7] Division of Geological and Planetary Sciences, 1200 E California Boulevard, Pasadena, CA 91125, USA
[8] Department of Astronomy, California Institute of Technology, Pasadena, CA 91125, USA
[9] Department of Earth and Planetary Sciences, University of California, Riverside, CA 92521, USA
[10] Department of Physics, California State University, San Marcos, CA 92096, USA
[11] Cahill Center for Astronomy & Astrophysics, California Institute of Technology, Pasadena, CA 91125, USA
[12] Sydney Institute for Astronomy (SIfA), School of Physics, University of Sydney, NSW 2006, Australia
[13] Centre for Astrophysics, University of Southern Queensland, Toowoomba, QLD, Australia
[14] Department of Physics & Astronomy, University of California Irvine, Irvine, CA 92697, USA
[15] Department of Physics & Astronomy, University of California Los Angeles, Los Angeles, CA 90095, USA
[16] Centre for Star and Planet Formation, Natural History Museum of Denmark & Niels Bohr Institute, University of Copenhagen, Øster Voldgade 5-7, DK-1350
Copenhagen K., Denmark
[17] Gemini Observatory/NSF's NOIRLab, 670 N. A'ohoku Place, Hilo, HI 96720, USA
[18] Department of Astronomy, Yale University, New Haven, CT 06511, USA
[19] Department of Physics and Astronomy, University of Notre Dame, Notre Dame, IN 46556, USA
[20] Center for Astrophysics |Harvard & Smithsonian, 60 Garden Street, Cambridge, MA 02138, USA
[21] DTU Space, Technical University of Denmark, Elektrovej 328, DK-2800 Kgs. Lyngby, Denmark
[22] NASA Ames Research Center, Moffett Field, CA 94035, USA
[23] NASA Goddard Space Flight Center, 8800 Greenbelt Road, Greenbelt, MD 20771, USA
[24] SETI Institute, 189 Bernardo Avenue, Suite 200, Mountain View, CA 94043, USA
[25] Department of Physics and Kavli Institute for Astrophysics and Space Research, Massachusetts Institute of Technology, Cambridge, MA 02139, USA
[26] Centro de Astrobiología (CAB), CSIC-INTA, Depto. de Astrofísica, ESAC campus, 28692, Villanueva de la Cañada (Madrid), Spain
[27] Departamento de Matemática y Física Aplicadas, Facultad de Ingeniería, Universidad Católica de la Santísima Concepción, Alonso de Rivera 2850, Concepción,
Chile
[28] Department of Earth, Atmospheric and Planetary Sciences, Massachusetts Institute of Technology, Cambridge, MA 02139, USA
[29] Department of Aeronautics and Astronautics, MIT, 77 Massachusetts Avenue, Cambridge, MA 02139, USA
[30] Department of Physics and Astronomy, Vanderbilt University, Nashville, TN 37235, USA
[31] Planetary Discoveries, 28935 Via Adelena, Santa Clarita, CA 91354, USA
[32] Department of Astrophysical Sciences, Princeton University, Princeton, NJ 08544, USA

Abstract

We present and confirm TOI-1751 b, a transiting sub-Neptune orbiting a slightly evolved, solar-type, metal-poor star ($T_{\rm eff} = 5996 \pm 110$ K, $\log(g) = 4.2 \pm 0.1$, $V = 9.3$ mag, [Fe/H] $= -0.40 \pm 0.06$ dex) every 37.47 days. We use TESS photometry to measure a planet radius of $2.77^{+0.15}_{-0.07}\,R_\oplus$. We also use both Keck/HIRES and APF/Levy radial velocities (RV) to derive a planet mass of $14.5^{+3.15}_{-3.14}\,M_\oplus$, and thus a planet density of 3.6 ± 0.9 g cm^{-3}. There is also a long-period ($\sim$400 days) signal that is observed in only the Keck/HIRES data. We conclude that this long-period signal is not planetary in nature and is likely due to the window function of the Keck/HIRES observations. This highlights the role of complementary observations from multiple observatories to identify and exclude aliases

---

[33] NSF Graduate Research Fellow.
[34] Henry Norris Russell Fellow.
[35] NASA Sagan Fellow.
[36] NSF Astronomy and Astrophysics Postdoctoral Fellow.

in RV data. Finally, we investigate the potential compositions of this planet, including rocky and water-rich solutions, as well as theoretical irradiated ocean models. TOI-1751 b is a warm sub-Neptune with an equilibrium temperature of ∼820 K. As TOI-1751 is a metal-poor star, TOI-1751 b may have formed in a water-enriched formation environment. We thus favor a volatile-rich interior composition for this planet.

Unified Astronomy Thesaurus concepts: Radial velocity (1332); Exoplanet structure (495); Transit photometry (1709); Mini Neptunes (1063)

Supporting material: machine-readable table

1. Introduction

The Transiting Exoplanet Survey Satellite (TESS; Ricker et al. 2014) has discovered 415 confirmed exoplanets to date,[37] and has identified thousands of planet candidates. These planets join the extensive population of over 5500 known planets. With this sample, we can search for demographic trends in planet radii, masses, compositions, and occurrence and begin to probe the mechanisms of planet formation and evolution that govern the planets in our galaxy.

The most commonly detected exoplanets are those smaller than Neptune (1–4 $R_\oplus$, commonly referred to as sub-Neptunes and/or super-Earths[1]). TESS has discovered over 200 such planets, and $\gtrsim$75% of all confirmed planets with measured radii are smaller than 4 $R_\oplus$[1]. Population-level trends offer windows into these planets' evolution and formation.

One such feature is the radius gap, a valley in the distribution of planet radii near 1.8 $R_\oplus$ (Fulton et al. 2017). This feature may be explained by two distinct populations: primarily rocky planets with H/Heenvelopes, and planets with volatile-rich interiors and more voluminous envelopes (e.g., Venturini & Helled 2017; Zeng et al. 2019; Venturini et al. 2020; Izidoro et al. 2022). Lee et al. (2022) suggest the radius gap is imprinted on the planet population at early times through planet formation in gas-poor disks. Alternatively, Luque & Pallé (2022) posit that the two populations are distinct in density, rather than radius, around M dwarfs. In this framework, compositional differences between the populations are set by the materials available in their formation environments, suggesting distinct formation locations within their protoplanetary disks. Water-rich planets may form beyond the snow line and then migrate inwards (Léger et al. 2004; Bitsch et al. 2019). On the other hand, rocky planets may form in situ from ice-poor pebbles and accrete primordial atmospheres from their natal disks (Chiang & Laughlin 2013; Lee & Chiang 2016).

Other mechanisms involving the sculpting of a single underlying population to create the radius gap have also been suggested. These include atmospheric mass loss through X-ray and ultraviolet or XUV-driven photoevaporation (Owen & Wu 2013; Rogers et al. 2021), core-powered mass loss (Ginzburg et al. 2018), and atmospheric mass loss and growth through giant impacts (Wyatt et al. 2020).

In this paper, we present and confirm TOI-1751 b, a sub-Neptune with a period of 37.47 days, orbiting a slightly evolved G0 star. TOI-1751 b is at the upper radius boundary of the sub-Neptune population, where planet occurrence begins to decrease. While much work has been done to investigate the mechanism(s) sculpting the radius gap, there are few models to explain this "occurrence cliff" (Dattilo et al. 2023). By characterizing planets in this regime, we may refine models that encapsulate both the radius gap and occurrence cliff.

Furthermore, due to the lower transit probability for planets with longer periods, only about 10% of sub-Neptunes confirmed by TESS have orbital periods greater than 25 days. TOI-1751 b thus resides in a population that is challenging to probe with transit surveys.

This target was observed by the TESS-Keck Survey (TKS), a collaboration spanning several institutions that pools time on the Keck I telescope on Maunakea. It was initially selected for radial velocity (RV) observations under several science cases: searching for distant giants, probing planets across the radius gap, and analyzing the diversity of gaseous envelopes (see Chontos et al. 2022 for a comprehensive of the TKS science cases). In Section 2 we discuss the data collected for this target. In Section 3 we characterize the stellar host. Section 4 presents our photometric and RV analyses and resulting planet parameters. In Section 5 we put this system in context and discuss possible planetary compositions, and conclude in Section 6.

2. Data Collected

2.1. Photometric Observations

The TESS mission observed TOI-1751 (TIC 287080092, HD 146757) for a total of 27 sectors (15, 17–26, 40–41, and 47–59) between 2019 August 15 and 2022 December 23 at 120 s cadence. The Science Processing Operations Center (SPOC; Jenkins et al. 2016) conducted a transit search of Sectors 15, 17, 18, and 19 on 2020 January 24 with an adaptive, noise-compensating matched filter (Jenkins 2002; Jenkins et al. 2010, 2020). This produced a threshold-crossing event (TCE) to which an initial limb-darkened transit model was fit (Li et al. 2019). Diagnostic tests were then conducted to investigate the planetary nature of the signal (Twicken et al. 2018). The transit signal passed all of the diagnostic tests. The TESS Science Office (TSO) reviewed the vetting information and issued an alert on 2020 February 27 (Guerrero et al. 2021). The signal was repeatedly recovered as additional observations were made in sectors 20–26, 40–41, and 47–59. The final transit search located the host star within $5\rlap.{''}8 \pm 3\rlap.{''}6$ of the source of the transit signal using a difference image centroiding test. We note that observations taken in sectors 15 and 17–26 were impacted by a bias in the sky background correction algorithm, which tended to overestimate the sky background flux. However, the impact on the derived planetary radius of TOI-1751 b is below 0.4% in all affected sectors and typically between 0.1% and 0.2%, so this is not a dominant error source in our analysis.

The target was also observed at 1800 s cadence in sector 16 and processed from Full-Frame Images (FFIs) through the Quick Look Pipeline (Huang et al. 2020a, 2020b). During sectors 56–59, TOI-1751 was also observed at 20 s cadence. This target was part of the following TESS Guest Observer programs: G04242 (PI: Mayo), G04191 (PI: Burt), G04039 (PI: Davenport), and G05144 (20 s target, PI: Huber).

2.2. Imaging Observations

Eclipsing binaries with small projected separations from a putative planet host star can create a false-positive transit signal. This effect is particularly important to consider for TESS Objects of Interest (TOIs) due to the TESS mission's larger pixel size ($21'' \times 21''$) compared to that of Kepler ($4'' \times 4''$). The SPOC transit search of TOI-1751 was able to constrain the location of the transit event to within a TESS pixel (see Section 2.1), suggesting a blended eclipsing binary was not the cause of the transit events. However, the flux from companion stars can lead to underestimated planetary radii, overestimated bulk densities, and erroneous stellar parameters (Ciardi et al. 2015; Furlan et al. 2017). The contaminating flux from a nearby star may also inhibit the detection of shallow transits (Lester et al. 2021). We thus obtained high-resolution imaging observations of TOI-1751 to search for nearby companion stars.

2.2.1. Lucky Imaging

We obtained two observations of TOI-1751 with the AstraLux instrument (Hormuth et al. 2008) installed at the 2.2 m telescope in the Calar Alto Observatory (Almería, Spain) under average weather and atmospheric conditions (seeing around $1''$) on 2021 March 22 and September 14 with the SDSS z filter. AstraLux uses the lucky imaging technique to obtain thousands of short exposure frames and selects a few percent of these frames with the best Strehl ratio (Strehl 1902). We obtained 62,200 frames with an exposure time of 10 ms each and selected the best 10% for a final effective exposure time of 62.2 s. We used the final stacked image to obtain the contrast curve by using the `astrasens` code (Lillo-Box et al. 2012, 2014). The result provides a contrast of $\Delta z = 6.3$ mag for separations above $0''\!.5$ on the 2021 March 22. We found no additional sources in the field of view of the instrument ($3'' \times 3''$) within these sensitivity limits.

2.2.2. Speckle Imaging

TOI-1751 was observed on 2020 June 6 using the 'Alopeke speckle instrument on the Gemini North 8 m telescope (Scott et al. 2021). 'Alopeke provides simultaneous speckle imaging in two bands (562 and 832 nm). Three sets of 1000×0.06 s exposures were collected and subjected to Fourier analysis in the standard reduction pipeline (see Howell et al. 2011). The Fourier transform of the summed autocorrelation of each set of images is used to make a fringe image of the target, which is then used to reconstruct the image. We find no companions fainter than the target star by 4.58 mag at 562 nm and by 6.73 mag at 832 nm at separations of $0''\!.5$ (i.e., 57 au) or greater.

2.2.3. Adaptive Optics Imaging

We used the Shane Adaptive optics infraRed Camera-Spectrograph (ShARCS, Kupke et al. 2012; Gavel et al. 2014) mounted on the 3 m Shane Telescope at Lick Observatory to collect AO imaging of TOI-1751. We observed the target using the K_s and J band filters. We conducted observations using a four-point dither pattern with a spacing of $4''$ on each side. We analyzed the data using the Stellar Image Maturation via Efficient Reduction (SImMER) package (Hirsch et al. 2019; Savel et al. 2020). We find no stellar companions within 5 mag at separations $\geqslant 1''$ in K_s band.

2.3. Spectroscopic Observations

2.3.1. Reconnaissance Spectra

We obtained one reconnaissance spectrum with an exposure time of 750 s on 2020 March 2 using the Tillinghast Reflector Echelle Spectrograph (TRES, Fűrész 2008) as part of the TESS Follow-up Observing Program (TFOP) SubGroup 2 (SG2) Reconnaissance Spectroscopy program. TRES is a fiber-fed echelle spectrograph on the 1.5 m Tillinghast Reflector at the Fred Lawrence Whipple Observatory (FLWO) in Arizona, USA, operating between 390 and 910 nm. The spectrograph has a resolving power of $R \sim 44{,}000$. We used the Stellar Parameter Classification (SPC; Buchhave et al. 2012) tool to derive stellar parameters. SPC cross-correlates a ~ 310 Å region of the observed spectrum surrounding the Mg b lines against a library grid of synthetic spectra calculated using the Kurucz (1992) atmospheric models to derive effective temperature ($T_{\rm eff}$), surface gravity, ($\log(g)$), rotational velocity, ($v \sin(i)$), and metallicity, ([m/H]). Metallicity is derived using all available metal lines and is therefore reported as [m/H].

We also obtained follow-up spectra for stellar classification with Las Cumbres Observatory's Network of Robotic Echelle Spectrographs (LCO/NRES, Siverd et al. 2018). NRES is a network of four identical spectrographs located at different observatories spanning a wide longitudinal range. Each instrument is a fiber-fed echelle spectrograph operating between 380 and 860 nm with a resolution of $R \sim 53{,}000$. Specifically, we obtained spectra for TOI-1751 at our NRES facility at the Wise Observatory, Israel, on 2020 March 4 at 23:00 UTC. The exposure time was 1800 s and the final SNR was 36 at 5500 Å. The wavelength-calibrated spectrum was obtained through the standard BANZAI-NRES pipeline (Brandt et al. 2020). The resulting stellar parameters from these observations are reported in Table 1.

2.3.2. Keck/HIRES

The HIgh Resolution Echelle Spectrometer (HIRES) on the Keck I telescope on Maunakea operates between 360 and 800 nm. We used Keck/HIRES to collect high-resolution spectra of TOI-1751 in order to derive precision RVs. We collected 71 spectra between 2020 and 2023 July. We observed TOI-1751 using the red cross-disperser, B5 decker ($3''\!.5 \times 0''\!.861$, $R = 50{,}000$) or C2 decker ($14'' \times 0''\!.861$, $R = 50{,}000$), and a median exposure time of 382 s. We took 69 RV observations with a warm ($50°$ C) iodine cell in the light path for wavelength calibrations as per Butler et al. (1996). We also took two further higher-resolution spectra without the iodine cell in the light path ("iodine-out") in 2020 March and September in order to obtain a spectral template, one using the B3 decker ($14'' \times 0''\!.574$, $R = 72{,}000$) and one using the C2 decker. The spectra were reduced using the standard procedures described in Howard et al. (2010). The RVs, RV errors, and Mount Wilson S-Index (a proxy for stellar activity derived from Ca II H & K lines) are reported in Table 4, and the RV data are shown in Figure 1. We also derived stellar parameters for TOI-1751 using these data (see Section 3, Table 1).

2.3.3. APF/Levy

The Automated Planet Finder (APF; Radovan et al. 2014) is a robotic 2.4 m telescope that hosts the Levy spectrograph, a high-resolution ($R = 100{,}000$) echelle spectrograph that operates

Table 1
TOI-1751 Stellar Parameters

Parameter	Value	Error	Source	Adopted?
Other Names	TIC 287080092	...	TIC v8.2[a]	...
	HD 146757	...	Henry Draper Catalog (Cannon & Pickering 1921)	...
	TYC 4192-02025-1	...	TYCHO (Høg et al. 2000)	...
Right Ascension (hh:mm:ss)	16:13:57.31	...	TIC v8.2[a]	...
Declination (hh:mm:ss)	+63:32:03.39	...	TIC v8.2[a]	...
V magnitude	9.327	0.003	TIC v8.2[a]	...
TESS magnitude	8.80616	0.006	TIC v8.2[a]	...
J magnitude	8.251	0.021	TIC v8.2[a]	...
K magnitude	7.934	0.027	TIC v8.2[a]	...
Gaia magnitude	9.19	...	Gaia DR3[b]	...
Parallax (mas)	8.809	0.009	Gaia DR3[b]	...
R.A. proper motion (mas yr^{-1})	8.60	0.01	Gaia DR3[b]	...
decl. proper motion (mas yr^{-1})	−172.84	0.02	Gaia DR3[b]	...
Radius ($R_\odot$)	1.17	0.18	SpecMatch-Empirical[c]	Y
Radius ($R_\odot$)	1.34	0.03	SpecMatch-Synthetic[d]	...
Radius ($R_\odot$)	1.27	0.06	TIC v8.2[a]	...
Radius ($R_\odot$)	1.01	0.11	LCO/NRES	...
Radius ($R_\odot$)	1.284	0.044	SED	...
Mass ($M_\odot$)	0.90	0.03	SpecMatch-Empirical[c]	Y
Mass ($M_\odot$)	0.89	0.03	SpecMatch-Synthetic[d]	...
Mass ($M_\odot$)	1.152	0.1689	TIC v8.2[a]	...
Mass ($M_\odot$)	0.925	0.044	LCO/NRES	...
Mass ($M_\odot$)	1.06	0.06	Empirical relations (Torres et al. 2010)	...
T_{eff}(K)	5996	110	SpecMatch-Empirical[c]	Y
T_{eff}(K)	5918	100	SpecMatch-Synthetic[d]	...
T_{eff}(K)	6114	122	TIC v8.2[a]	...
T_{eff}(K)	5850	50	NOT/FIES	...
T_{eff}(K)	5801	50	FLWO/TRES	...
T_{eff}(K)	6049	100	LCO/NRES	...
T_{eff}(K)	6075	75	SED	...
$\log(g)$	4.24	0.10	SpecMatch-Synthetic[c]	Y
$\log(g)$	4.293	0.084	TIC v8.2[a]	...
$\log(g)$	4.1	0.1	NOT/FIRES	...
$\log(g)$	4.0	0.1	FLWO/TRES	...
$\log(g)$	4.4	0.1	LCO/NRES	...
$v \sin i$ (km s^{-1})	1.27	1.0	SpecMatch-Empirical[c]	Y
$v \sin i$ (km s^{-1})	3.74	0.50	NOT/FIRES	...
$v \sin i$ (km s^{-1})	4.29	0.5	FLWO/TRES	...
$v \sin i$ (km s^{-1})	2.49	0.62	LCO/NRES	...
$P_{rot}/\sin(i)(d)$	46	37	Calculated using $v \sin i$ and R_*	...
$P_{rot}/\sin(i)(d)$	50.9	40.1	Empirical relations (Torres et al. 2010)	...
$P_{rot}(d)$	23.3	3.2	Predicted using $\log R'_{HK}$ (Mamajek & Hillenbrand 2008)	...
[Fe/H] (dex)	−0.40	0.06	SpecMatch-Empirical[c]	Y
[Fe/H] (dex)	−0.50	0.09	SpecMatch-Synthetic[c]	...
[Fe/H] (dex)	−0.33	0.06	LCO/NRES	...
[Fe/H] (dex)	−0.5	0.2	SED	...
$\log R'_{HK}$	−5.244	0.212	APF/Levy	...
$\log R'_{HK}$	−5.149	0.071	Keck/HIRES	...
[m/H] (dex)	−0.429	0.08	NOT/FIRES	...
[m/H] (dex)	−0.389	0.08	FLWO/TRES	...
A_V	0.03	0.03	SED	...
Age (Gyr)	10.0	1.5	Empirical relations (Mamajek & Hillenbrand 2008)	...

Notes.
[a] TESS Input Catalog, Version 8.2 (Paegert et al. 2022).
[b] Gaia DR3 (Gaia Collaboration et al. 2023).
[c] SpecMatch-Empirical (Yee et al. 2017) applied to Keck/HIRES data.
[d] SpecMatch-Synthetic (Petigura et al. 2017) applied to Keck/HIRES data.

between 374 and 980 nm (Vogt et al. 2014). We obtained 129 observations of TOI-1751 using APF/Levy between 2020 April and 2023 January, with multiple observations per night on several nights. These observations had a median exposure time of 2100 s. Similarly to the Keck/HIRES observations, spectra were taken through a warm iodine cell for wavelength
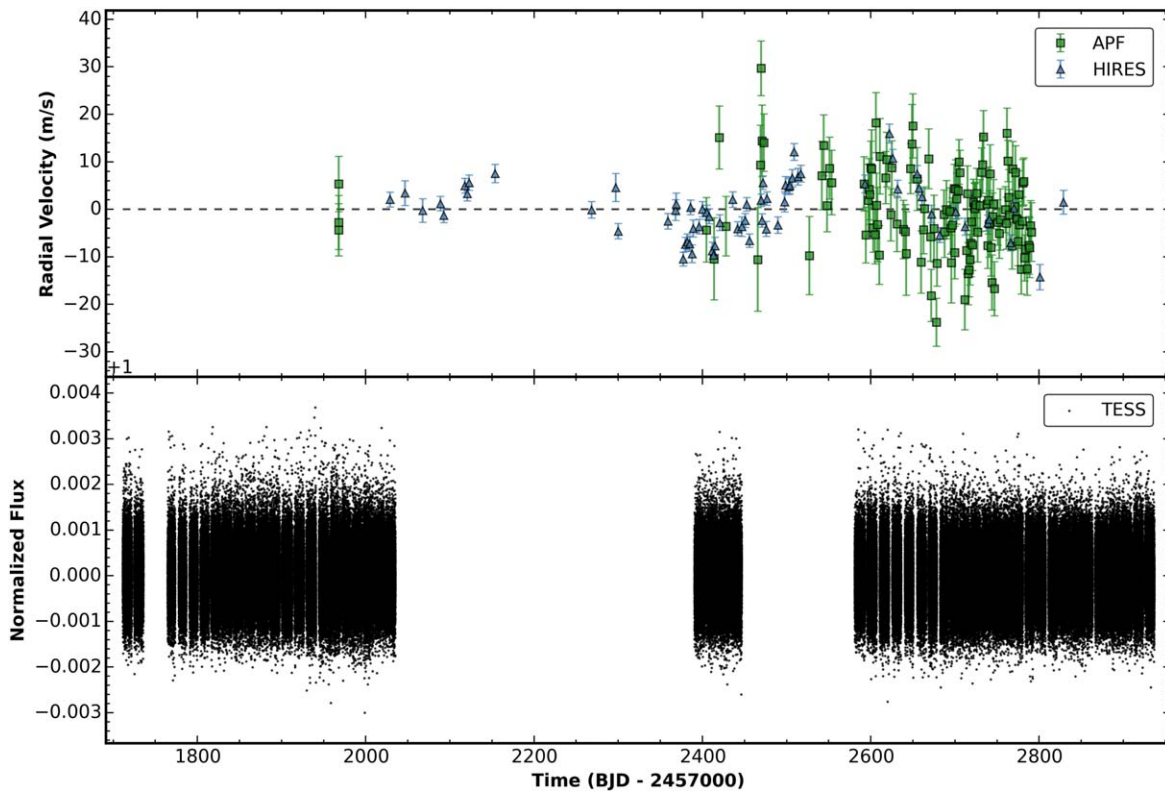
Figure 1. Top: RV measurements from APF/Levy (green squares) and Keck/HIRES (blue diamonds). For clarity, the RV offsets determined from the joint RV and transit fit (see Section 4.3) for each instrument have been subtracted from the data, and the respective jitter terms have been combined with the instrumental uncertainties to produce the error bars. Bottom: flattened and normalized TESS PDCSAP flux light curve.

calibration, and RVs were derived using the methods described in Howard et al. (2010). As with other faint targets on APF (V ∼9), we use the Keck template splined onto the APF wavelength solution to calculate precise RVs. We report the APF/Levy RVs in Table 4, and show the data in Figure 1.

3. Stellar Parameters

3.1. Spectroscopically Derived Parameters

We used the `SpecMatch-Emp`[38] algorithm (Yee et al. 2017) to characterize TOI-1751. `SpecMatch-Emp` uses a library of high resolution (R∼55,000) and high signal-to-noise (>100) Keck/HIRES spectra to measure stellar parameters from optical spectra. This method achieves accuracies of 100 K in effective temperature, 15% in stellar radius, and 0.09 dex in metallicity for FGK stars. The algorithm takes the observed stellar spectrum, shifts it to the rest frame wavelength scale, identifies the most similar library spectra, and interpolates between them to derive parameters for the target star. We measured a stellar mass of $0.90 \pm 0.03\ M_\odot$, a stellar radius of $1.17 \pm 0.18 R_\odot$, and an effective temperature of 5996 ± 110 K. We also used the `SpecMatch-Synthetic`[39] code (Petigura et al. 2017) to measure stellar parameters from the iodine-out Keck/HIRES spectrum by interpolating between a grid of model spectra from Coelho et al. (2005).

Additionally, we report stellar parameters derived from reconnaissance spectra (described in Section 2.3.1). However, we do not adopt these parameters in our analysis due to the

higher resolution of Keck/HIRES. Some of these parameters (e.g., $v \sin(i)$) are discrepant to greater than 2σ from those measured using Keck/HIRES data, likely due to the low-resolution and low-cadence (often 1 observation per instrument) nature of these observations. Our adopted parameters are consistent to 1σ with those derived homogeneously for the TKS sample in MacDougall et al. (2023).

We find that TOI-1751 is a slightly evolved ($\log g = 4.24 \pm 0.10$), metal-poor ([Fe/H] = -0.40 ± 0.06), solar-type star. The spectroscopic $v \sin i$ and $R_\star$ measured using `SpecMatch-Emp` imply a projected rotation period for the star of $P_{\rm rot}/\sin i = 46 \pm 37$ days. We derive additional estimates of the projected rotation period from the $\log R'_{\rm HK}$ observations, and using the spectral energy distribution (SED) of TOI-1751 (see Section 3.2). We report all calculated stellar parameters in Table 1.

3.2. Photometrically Derived Parameters

We also performed an analysis of the broadband SED of the star together with the Gaia DR3 parallax (Gaia Collaboration et al. 2023) in order to determine an empirical measurement of the stellar radius (Stassun & Torres 2016; Stassun et al. 2017, 2018). We pulled the JHK_S magnitudes from 2MASS (Skrutskie et al. 2006), the W1–W4 magnitudes from WISE (Wright et al. 2010), the $G_{\rm BP}G_{\rm RP}$ magnitudes from Gaia, and the far-ultraviolet and near-ultraviolet magnitudes from GALEX (Martin et al. 2005). Together, the available photometry spans the full stellar SED over the wavelength range 0.2–20 μm.

We performed a fit using PHOENIX stellar atmosphere models (Husser et al. 2013), varying effective temperature

---

[38] https://github.com/samuelyeewl/specmatch-emp
[39] github.com/petigura/specmatch-syn

($T_{\rm eff}$), metallicity ([Fe/H]), and extinction (A_V). We limited A_V to the maximum line-of-sight value from the Galactic dust maps of Schlegel et al. (1998). The resulting fit has a best fit $A_V = 0.03 \pm 0.03$, $T_{\rm eff} = 6075 \pm 75$ K, and [Fe/H] $= -0.5 \pm 0.2$, with a reduced χ^2 of 1.3. Integrating the unreddened model SED gives the bolometric flux at Earth, $F_{\rm bol} = 4.98 \pm 0.23 \times 10^{-9}$ erg s^{-1} cm^{-2}. Taking the $F_{\rm bol}$ together with the Gaia parallax directly gives the bolometric luminosity, $L_{\rm bol} = 2.000 \pm 0.094 \, L_\odot$. The Stefan–Boltzmann relation then gives the stellar radius, $R_\star = 1.284 \pm 0.044 \, R_\odot$. In addition, we estimated the stellar mass and projected stellar-rotation period using the empirical relations of Torres et al. (2010) ($M_\star = 1.06 \pm 0.06 \, M_\odot$, $P_{\rm rot}/\sin(i) = 50.9 \pm 40.1$ days).

We note that the stellar mass derived from the spectroscopic data ($0.90 \pm 0.03 \, M_\odot$) is inconsistent to 1.4σ with that reported in the TESS Input Catalog ($1.15 \pm 0.17 \, M_\odot$, TIC v8.2, Paegert et al. 2022), possibly due to the slightly evolved nature of the star.

We also do not see any evidence of stellar-rotation-related signals in the Lomb–Scargle periodogram (Lomb 1976; Scargle 1982) of the TESS light curve. The strongest power in the periodogram is at 4.46 days, but given the measured $v\sin(i)$ and $R_\star$ of this target (1.27 ± 1.00 km s^{-1}, $1.17 \pm 0.18 R_\star$), this is unlikely to correspond to stellar rotation, and may be due to TESS momentum dumps. We attribute the lack of photometric rotation signals to the known challenges with identifying rotation periods longer than the TESS orbital period of 13.7 days, or roughly half a sector length (Canto Martins et al. 2020; Fetherolf et al. 2023).

3.3. Constraining Stellar Age and Companions

To further investigate the rotation period and age of TOI-1751, we use the BANYAN Σ (Bayesian Analysis for Nearby Young AssociatioNs Σ; Gagné et al. 2018) analysis tool to investigate whether TOI-1751 is a member of any of the 27 known young stellar associations within 150 pc. We find that TOI-1751 is highly likely (99.9%) to not be a member of these associations, pointing to an older age. This is in line with the reported surface gravity, suggesting that TOI-1751 is nearing the end of its time on the main sequence.

We use the empirical activity-age relations of Mamajek & Hillenbrand (2008) along with the $\log R'_{\rm HK}$ of TOI-1751 to find an age of 10.0 ± 1.5 Gyr. This includes both the measurement uncertainty on $\log R'_{\rm HK}$ and the systematic error reported for the Mamajek & Hillenbrand (2008) relation. The same empirical relations of Mamajek & Hillenbrand (2008) predict a rotation period from the $\log R'_{\rm HK}$ of 23.3 ± 3.2 days. This is consistent with the $P_{\rm rot}/\sin i$ value determined using the Torres et al. (2010) empirical relations.

Additionally, Gaia DR3 (Gaia Collaboration et al. 2023) does not contain any proper motion companions within $100''$ of TOI-1751. We also used `tpfplotter` (Lillo-Box et al. 2014) to search for sources in GAIA DR3 within the pipeline aperture mask used to generate the light curve. We found that there were no contaminating sources up to 8 mag fainter than TOI-1751 within the aperture mask, and thus likely no substantial contaminating flux. Furthermore, GAIA DR3 reports a Renormalized Unit Weight Error (RUWE) of 0.90, indicating that this target does not have a detectable companion (Lindgren 2018).

3.4. Galactic Context

TOI-1751 is a high proper motion star, and we find that it is also metal-poor ([Fe/H] $= -0.40 \pm 0.06$). These attributes indicate that it may be a member of the thick disk of the Milky Way (Bensby 2004; Bensby & Feltzing 2010). Thick-disk stars are kinematically hotter, more depleted in metals, more enriched in alpha elements, and older than those in the thin disk. The formation of the thick disk is still unclear (van der Kruit & Freeman 2011), with possible mechanisms including the merger of the Milky Way with a dwarf galaxy (e.g., Quinn et al. 1993) and radial mixing of gas and stars (e.g., Schönrich & Binney 2009; Loebman et al. 2011). Planets orbiting thick-disk stars (e.g., Kepler-444; Campante et al. 2015) show that planet formation has occurred for $\gtrsim 11$ Gyr. Carrillo et al. (2020) calculated the galactic velocity of TIC stars and reported ($U_{\rm LSR}$, $V_{\rm LSR}$, $W_{\rm LSR}$) $= (106.2 \pm 0.2, \; -35.5 \pm 0.2, \; 1.6 \pm 0.2)$ km s^{-1}, with $v_{\rm tot} = (U_{\rm LSR}^2 + V_{\rm LSR}^2 + W_{\rm LSR}^2)^{\frac{1}{2}} \approx 110$ km s^{-1} for this target. This result is consistent with that calculated using the methods in Rodriguez (2016) and may suggest thick-disk membership (Nissen 2004). TOI-1751 is, however, still consistent with the low-metallicity tail of the thin-disk distribution and is 1.6 times more likely to belong to the thin disk than the thick disk (Carrillo et al. 2020). Therefore, we do not conclusively report its thick-disk membership and defer a detailed discussion of the star's alpha abundances to future work (Polanski et al.2024, in preparation).

4. Data Analysis

4.1. TESS Photometry Analysis

We used the `lightkurve` package (Lightkurve Collaboration et al. 2018) to download the 2 minutes SPOC TESS light curves for TOI-1751. We normalized and stitched together the light curves from each TESS Sector (see Figure 1) and computed a box least-squares (BLS; Kovács et al. 2002) periodogram. We recovered a significant periodic signal at 37.468 days with an associated Signal Detection Efficiency (SDE) of 24.8. This signal corresponds to the planet candidate TOI-1751.01.

We visually inspected the light curve to confirm the time of the first transit of TOI-1751.01. Next, we reduced the computation time for the subsequent transit fit using the BLS period to trim data points falling outside of a 2 day window on either side of each transit center. We also removed any observations flagged with a quality flag greater than 0 to exclude scattered light, cosmic rays, and additional anomalous events.

Next, we flattened each transit individually by first fitting a second-order polynomial to the out-of-transit baseline flux spanning 12–48 hr before and after each transit midpoint. We then divided out the best-fit polynomial from the Presearch Data Conditioning Simple Aperture Photometry (PDCSAP; Smith et al. 2012; Stumpe et al. 2012, 2014) flux within the full 4 day window for each transit. To ensure robust flattening, we required each 4 day window to be at least 80% complete (i.e., at least 80% of possible cadences contained data). This resulted in 13 complete flattened transits.

To constrain the size and orbital properties of TOI-1751 b, we modeled the transit photometry using the `exoplanet` package (Foreman-Mackey et al. 2021). To remain agnostic to the stellar properties, we defined a transit model in terms of the planet-to-star radius ratio ($R_p/R_\star$), time of first transit (T_0),

orbital period (P), semimajor axis in units of stellar radii (a/R_*), impact parameter (b), and quadratic limb-darkening coefficients (q_1, q_2, using the parameterization of Kipping 2013). Our model also included a mean baseline flux term ($\langle F \rangle$) and a photometric jitter term (s), which was added in quadrature to the reported flux uncertainties. Finally, we assumed a circular orbit for the planet, setting the eccentricity equal to zero.

We optimized the model parameters using Bayesian inference, implementing a Hamiltonian Monte Carlo (HMC) No U-Turn Sampler (NUTS; Hoffman & Gelman 2011) with PyMC3 (Salvatier et al. 2016) to sample the posterior probability distributions. The prior distributions we selected for each parameter are given in Table 2. We set the target acceptance rate to 0.95 (to account for the higher acceptance fractions returned by HMC samplers compared with Metropolis–Hastings samplers) and initialized the sampler by adapting a dense mass matrix from the sample covariances. We then ran the sampler using a total of four chains, each one drawing 20,000 samples after discarding 5000 burn-in steps. To check for convergence, we computed the Gelman–Rubin Diagnostic and visually inspected the sampler trace plot for each parameter. The median and 68% confidence range for each parameter are given in Table 2.

4.2. RV Analysis

We analyze the combined Keck/HIRES and APF/Levy RV observations in order to confirm TOI-1751.01. The Lomb–Scargle periodogram of the combined Keck/HIRES and APF/Levy RV data (see Figure 2) shows a significant peak with <0.1% false alarm probability at 37.4 days, which we confirm as the exoplanet TOI-1751 b. We also note a peak at ∼400 days. This second, longer-period signal may indicate the presence of a nontransiting distant giant planet in the system.

We used the RadVel package (Fulton et al. 2018), which fits Keplerian models using maximum posterior probability optimization to model the RV data. In our models, we allowed several combinations of the orbital period (P), time of conjunction (t_c), mass (M_{pl}), argument of periastron (ω), and eccentricity (e) of the planet (s) to vary. We performed several fits: including or excluding a linear trend ($\dot{\gamma}$), including or excluding a second planet at ∼400 days, and circular or eccentric orbits. In all cases, we fixed the orbital period (P_b) and time of conjunction ($t_{c,b}$) using the precise constraints from our initial photometric analysis (see Section 4.1).

We find that the mass of TOI-1751 b is consistent to 1σ across all models. Furthermore, the mass is consistent to 1σ when fitting the Keck/HIRES and APF/Levy data separately. The preferred model using the full data set is a circular one-planet model, which returns a minimum mass of $14.5^{+3.15}_{-3.14}\,M_\oplus$ for TOI-1751 b. The ΔBIC between the circular model and the eccentric model is less than 1, so there is no clear evidence for eccentricity (Kass & Raftery 1995). We report the circular posteriors in Table 2.

4.2.1. Evidence Against a Distant Giant Planet

There is much interest in probing the outer regions of planetary systems, and investigating the occurrence of small, inner planets that may depend on the presence of distant giants (e.g., Zhu & Wu 2018; Van Zandt et al. 2023). We find that the

∼400 day periodic signal seen in the combined data set is only present in the Keck/HIRES RVs, and is not seen in the APF/Levy data (see Figure 2). This casts doubt on a planetary interpretation of the 400 day signal.

In order to investigate whether a distant giant planet would be detected in the APF/Levy data, we simulated observations using parameters for TOI-1751 b and the putative outer planet determined from a two-planet Keck/HIRES-only fit. We used $M = 14.9 \pm 3.8 M_\oplus$ for the inner planet and $M = 88 \pm 15 M_\oplus$ (∼0.9 $M_{\rm Saturn}$) for the outer planet to simulate 129 observations, using real APF/Levy observational time stamps and errors. All of the simulated observations show a long-period peak greater than that in the real APF/Levy data (see Figure 3). This suggests that if such a distant giant planet were present in the system, its signal would have been captured by the APF observations. We performed a similar exercise for simulated APF data assuming lower masses (10, 35, and 50 $M_\oplus$) for a putative distant giant. None of these scenarios reproduced the periodogram of the APF data. We used Radvel to model these sets of simulated observations. The measured planet mass for the outer planet is inconsistent with the injected values. As such, we did not find a planetary solution for the 400 day signal that is consistent with observations of TOI-1751 b, and we conclude that this long-period signal is not planetary in nature.

A possible cause of this spurious signal is that the stellar template used in reducing the RV observations was suboptimal. This would cause a correlation between the barycentric velocity of the observations and the RV measurements. However, we would expect such an effect to impact the APF/Levy observations as well. We also computed the spectral window function of our observations, i.e., the Lomb–Scargle periodogram of observation times. There is substantial power at ∼200 days in the window function of the Keck/HIRES observations, indicating that the periodic signal in the RV data may be a harmonic signal in the window function due to patterns in observation times. Given that the ∼400 day periodic signal is only present in the Keck/HIRES data, that it would be detectable in the APF/Levy data assuming it was astrophysical, and that there is a corresponding peak in the Keck/HIRES window function, we conclude that this signal is not planetary in nature. This highlights the valuable role that the APF, and other comparable telescopes, can play in large RV surveys. High-cadence APF/Levy observations of TOI-1751, despite being lower precision than the Keck/HIRES data, allowed us to identify and remove an alias in our data and to gain a clearer picture of this system.

4.3. Joint Photometry and RV Analysis

Using the results from Sections 4.1 and 4.2 as a baseline, we performed a joint fit of the 13 flattened TESS transits described in Section 4.1 and the APF and HIRES RV measurements described in Section 4.2.

As in Section 4.1, we used the exoplanet package (Foreman-Mackey et al. 2021). We define the combined photometry and RV model by a set of 16 free parameters: R_p/R_*, T_0, P, b, q_1, q_2, and $\langle F \rangle$ (as in the transit-only model), as well as stellar mass and radius, M_* and R_*, and planet mass M_p. We also included three jitter terms (one per instrument), which were added to the respective instrument uncertainties in quadrature, as well as RV offsets, γ, for both APF and HIRES. Finally, we added an RV acceleration term, $\dot{\gamma}$. We also derived the following quantities from the fit parameters: the stellar

Table 2
Prior Distributions and Posterior Quantiles Derived from Model Fits

Parameter	RV-only Fit		Transit-only Fit		RV+transit Fit (Eccentric)		RV+transit Fit (Circular)	
	Prior	Posterior median[a]	Prior	Posterior median[a]	Prior	Posterior median[a]	Prior	Posterior median[a]
Stellar parameters								
Stellar mass, $M_\star$ ($M_\odot$)	⋯	0.90 ± 0.03	⋯	⋯	$\mathcal{T}(0.90, 0.03, 0, 3)$	0.90 ± 0.03	$\mathcal{T}(0.90, 0.03, 0, 3)$	0.90 ± 0.03
Stellar radius, $R_\star$ ($R_\odot$)	⋯	⋯	⋯	⋯	$\mathcal{T}(1.17, 0.18, 0, 3)$	$1.21^{+0.12}_{-0.12}$	$\mathcal{T}(1.17, 0.18, 0, 3)$	$1.20^{+0.06}_{-0.03}$
Stellar bulk density, $\rho_\star$ (g cm^{-3})	⋯	⋯	⋯	⋯	⋯	$0.72^{+0.26}_{-0.18}$	⋯	$0.74^{+0.05}_{-0.10}$
Mean flux, $\langle F \rangle$	⋯	⋯	$\mathcal{N}(1.00, 0.01)$	0.999998 ± 0.000003	$\mathcal{N}(1.00, 0.01)$	0.999998 ± 0.000003	$\mathcal{N}(1.00, 0.01)$	0.999998 ± 0.000003
[b]Quadratic limb-darkening coeff., q_1	⋯	⋯	$\mathcal{U}(0, 1)$	$0.30^{+0.14}_{-0.17}$	$\mathcal{U}(0, 1)$	$0.29^{+0.14}_{-0.16}$	$\mathcal{U}(0, 1)$	$0.29^{+0.14}_{-0.16}$
[b]Quadratic limb-darkening coeff., q_2	⋯	⋯	$\mathcal{U}(0, 1)$	$0.26^{+0.28}_{-0.19}$	$\mathcal{U}(0, 1)$	$0.24^{+0.26}_{-0.17}$	$\mathcal{U}(0, 1)$	$0.24^{+0.26}_{-0.17}$
Planet parameters								
Planet-to-star radius ratio, $R_p/R_\star$	⋯	⋯	$\mathcal{L}(-3.86, 0.01)$	0.02110 ± 0.00019	$\mathcal{N}(0.0211, 0.0002)$	0.02119 ± 0.00017	$\mathcal{N}(0.0211, 0.0002)$	0.02119 ± 0.00017
Planet radius, R_p ($R_\oplus$)	⋯	⋯	⋯	⋯	⋯	$2.79^{+0.29}_{-0.27}$	⋯	$2.77^{+0.15}_{-0.07}$
Planet mass, M_p ($M_\oplus$)	>0	17.6 ± 3.5	⋯	⋯	$\mathcal{L}(2.8, 2.0)$	17.1 ± 3.2	$\mathcal{L}(2.8, 2.0)$	$14.5^{+3.15}_{-3.14}$
Planet bulk density, ρ_p (g cm^{-3})	⋯	⋯	⋯	⋯	⋯	$4.2^{+1.8}_{-1.3}$	⋯	3.6 ± 0.9
Orbital parameters								
Orbital period, P (days)	=37.468	37.468	$\mathcal{L}(3.62, 0.01)$	$37.46850^{+0.00011}_{-0.00009}$	$\mathcal{L}(3.62, 0.01)$	$37.468489^{+0.000082}_{-0.000074}$	$\mathcal{L}(3.62, 0.01)$	$37.468490^{+0.000082}_{-0.000075}$
First transit center, T_0 ($BJD - 2457000$)	⋯	⋯	$\mathcal{N}(1733.6, 0.1)$	$1733.6349^{+0.0019}_{-0.0025}$	$\mathcal{N}(1733.635, 0.0001)$	$1733.6351^{+0.0013}_{-0.0015}$	$\mathcal{N}(1733.635, 0.0001)$	$1733.6352^{+0.0014}_{-0.0015}$
Transit duration, $T_{\rm dur}$ (hr)	⋯	⋯	⋯	⋯	⋯	$9.5^{+1.4}_{-1.3}$	⋯	$7.5^{+0.08}_{-0.06}$
Semimajor axis, $a/R_\star$	⋯	⋯	$\mathcal{U}(10, 60)$	$37.92^{+0.86}_{-1.97}$	⋯	$37.6^{+4.0}_{-3.5}$	⋯	$38.0^{+0.8}_{-1.8}$
Semimajor axis, a(au)	⋯	$0.2116^{+0.0023}_{-0.0024}$	⋯	⋯	⋯	$0.2115^{+0.0023}_{-0.0024}$	⋯	0.2116 ± 0.0023
Impact parameter, b	⋯	⋯	$\mathcal{U}(0, 1)$	$0.20^{+0.17}_{-0.13}$	$\mathcal{U}(0, 1)$	$0.20^{+0.16}_{-0.14}$	$\mathcal{U}(0, 1)$	$0.20^{+0.16}_{-0.14}$
Eccentricity, e	=0.0	0.0	0.0	0.0	$\mathcal{U}(0, 1)$	$0.261^{+0.077}_{-0.090}$	0.0	0.0
Argument of periastron, ω (rad)	⋯	$2.82^{+0.58}_{-0.47}$	0.0	0.0	$\mathcal{U}(0, 2\pi)$	$3.29^{+0.41}_{-0.44}$	0.0	0.0
Other parameters								
RV semiamplitude, K (m s^{-1})	⋯	$3.88^{+0.82}_{-0.8}$	⋯	⋯	⋯	$3.64^{+0.68}_{-0.69}$	⋯	2.98 ± 0.64
[c]HIRES offset, $\gamma_{\rm HIRES}$ (m s^{-1})	⋯	-0.18 ± 0.66	⋯	⋯	$\mathcal{N}(0.0, 1.0)$	$-0.49^{+0.55}_{-0.54}$	$\mathcal{N}(0.0, 1.0)$	-0.52 ± 0.54
[c]APF offset, $\gamma_{\rm APF}$ (m s^{-1})	⋯	-0.39 ± 0.72	⋯	⋯	$\mathcal{N}(0.0, 1.0)$	0.52 ± 0.57	$\mathcal{N}(0.0, 1.0)$	0.43 ± 0.58
[c]Background acceleration, $\dot\gamma$ (m s^{-1} d^{-1})	⋯	$-0.007^{+0.0029}_{-0.003}$	⋯	⋯	$\mathcal{N}(0.0, 1.0)$	-0.0067 ± 0.0023	$\mathcal{N}(0.0, 1.0)$	-0.0069 ± 0.0023
[d]TESS jitter, log $s_{\rm TESS}$	⋯	⋯	$\mathcal{N}(-7.45, 10)$	$-8.968^{+0.069}_{-0.081}$	$\mathcal{N}(-7.45, 10)$	$-8.968^{+0.069}_{-0.080}$	$\mathcal{N}(-7.45, 10)$	$-8.969^{+0.070}_{-0.081}$
[d]HIRES jitter, log $s_{\rm HIRES}$ (m s^{-1})	$\mathcal{U}(-20, 20)$	$5.0^{+0.56}_{-0.47}$	⋯	⋯	$\mathcal{N}(0.52, 5)$	1.60 ± 0.10	$\mathcal{N}(0.52, 5)$	1.58 ± 0.10
[d]APF jitter, log $s_{\rm APF}$ (m s^{-1})	$\mathcal{U}(-20, 20)$	$5.5^{+0.77}_{-0.75}$	⋯	⋯	$\mathcal{N}(1.74, 5)$	$1.59^{+0.13}_{-0.14}$	$\mathcal{N}(1.74, 5)$	$1.67^{+0.12}_{-0.13}$

Notes. $\mathcal{U}(a, b)$ is a uniform distribution that is nonzero only between a and b; $\mathcal{N}(\mu, \sigma)$ is a normal distribution with mean μ and standard deviation σ; $\mathcal{T}(\mu, \sigma, a, b)$ is a truncated normal distribution with mean μ and standard deviation σ, bounded between a and b; and $\mathcal{L}(\mu, \sigma)$ is a lognormal distribution with log mean μ and log standard deviation σ.

[a] Median posterior values are shown with the 68% confidence interval.

[b] The quadratic limb-darkening coefficients are implemented using the Kipping (2013) parameterization.

[c] The RV trend coefficients are for a linear function: $v_r(t) = \dot\gamma t + \gamma$.

[d] Each jitter term was added to the respective data uncertainties in quadrature, such that the effective error was $\sqrt{\sigma^2 + s^2}$.
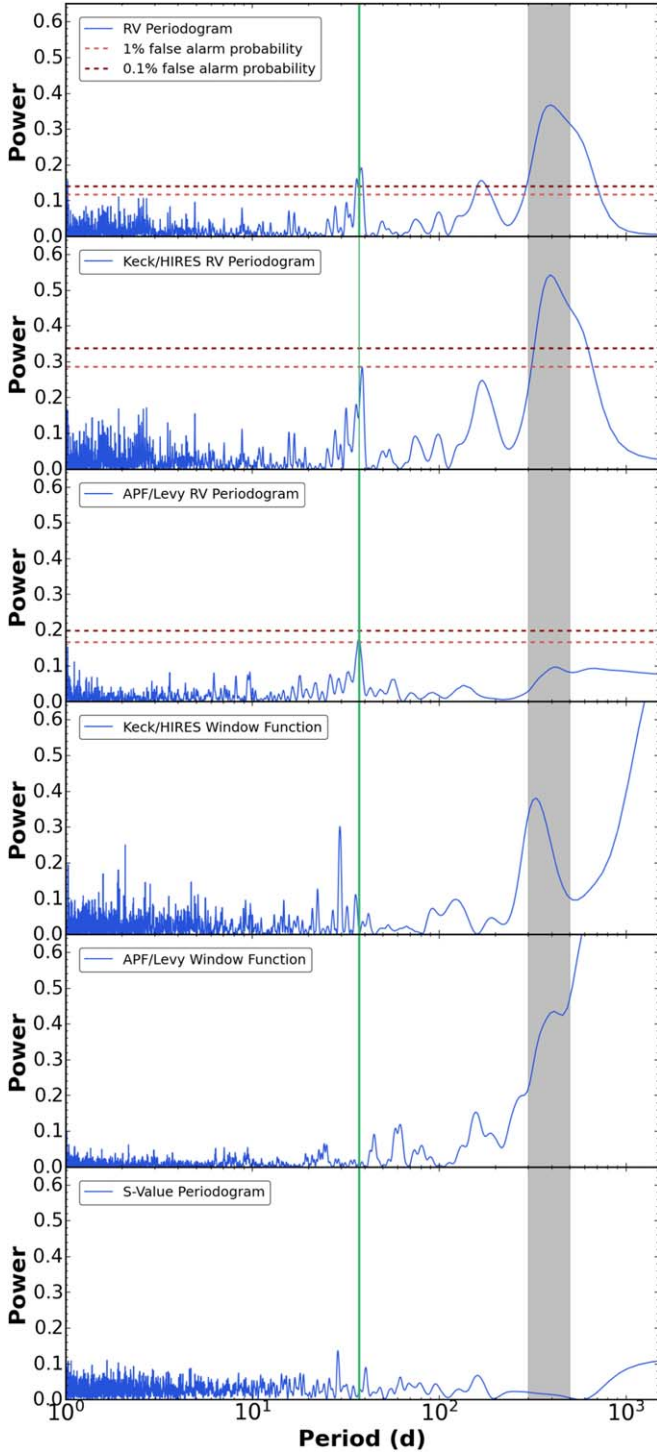
Figure 2. Lomb–Scargle periodogram of (a) all RV observations, (b) Keck/HIRES RVs, (c) APF/Levy RVs, (d) Keck/HIRES window function, (e) APF/Levy window function, and (f) S-values. The vertical green line marks the 37 day period, and the gray-shaded region marks the 300–500 day range. The long-period peak seen in the periodogram of the full RV data set is not present in the APF data, and is at a period similar to that of a significant peak in the HIRES window function. The dark red dashed line represents the 0.1% false alarm level. Data consisting of Gaussian noise with no periodic signal would produce peaks of this height (or above) in <0.1% of samples. The red dashed line is the 1% false alarm level.

density (ρ_*), planet radius (R_p), planet bulk density (ρ_p), RV semiamplitude (K), transit duration (t_{dur}), and semimajor axis (a). As stated in Section 4.2, the ΔBIC between circular and
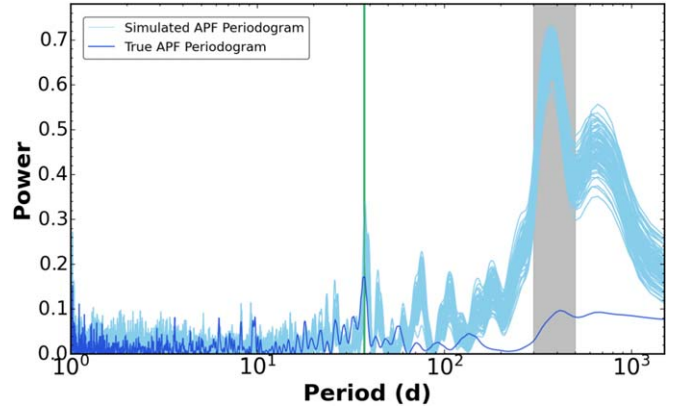
Figure 3. Lomb–Scargle periodogram of APF/Levy RV data (blue) and 100 simulations of APF/Levy observations of a two-planet TOI-1751 system. The period of TOI-1751 b is indicated by a vertical green line. The peaks in the periodogram of the simulated data are consistently higher than those of the real data at ∼400 days.

eccentric is less than 1, indicating no clear evidence for eccentricity, so we adopt the circular model posteriors. We report both circular and eccentric model posteriors in Table 2 for completeness.

Again, we used the HMC NUTS implemented in PyMC3 (Salvatier et al. 2016) to optimize the model parameters and sample their posterior probability distributions. The priors we adopted for each of these parameters are shown in Table 2. We followed the procedure described in Section 4.1 to initialize the sampler and sample the posteriors. The full posterior distributions for the joint transit and RV fit are shown in Figure 8 in the Appendix, and the posteriors for the auxiliary parameters are shown in Figure 9. Finally, phase-folded plots of the data and models are shown in Figures 4 and 5. The median posterior values for each parameter, along with 68% confidence intervals, are shown in Table 2. We confirm the planetary nature of TOI-1751 b, and measure its radius ($2.77^{+0.15}_{-0.07} R_\oplus$), mass ($14.5^{+3.15}_{-3.14} M_\oplus$), and bulk density ($3.6 \pm 0.9 \, \mathrm{g \, cm^{-3}}$).

5. Discussion

5.1. TOI-1751 b in Context

Looking to our solar system, the ice giant planets Uranus and Neptune are the most similar to TOI-1751 b in mass. However, their internal compositions, gravitational fields, rotation periods, and atmospheric dynamics are poorly constrained (Podolak & Helled 2012; Neuenschwander & Helled 2022; Miguel & Vazan 2023). These substantial uncertainties about ice giant interiors inhibit the use of solar system benchmarks to inform models of extrasolar planets.

TOI-1751 b has a longer orbital period (37.47 days) than ∼90% of all confirmed planets with measured radii consistent to 1σ with TOI-1751 b and with well-constrained masses ($\frac{M_{pl}}{\sigma_{M_{pl}}} > 3$). Additionally, it has a larger mass than 94% of this sample (see Figure 6). It is also one of only five sub-Neptunes with periods longer than 30 days orbiting bright ($V < 10$) stars, representing one of the best cases for investigating the warm sub-Neptune population.

TOI-1751 b is in a similar region of mass–radius space to several confirmed planets: TOI-561 d (Lacedelli et al. 2021), TOI-1052 b (Armstrong et al. 2023), TOI-1260 c (Georgieva et al. 2021), Kepler-48 c (Steffen et al. 2013), Kepler-107 e
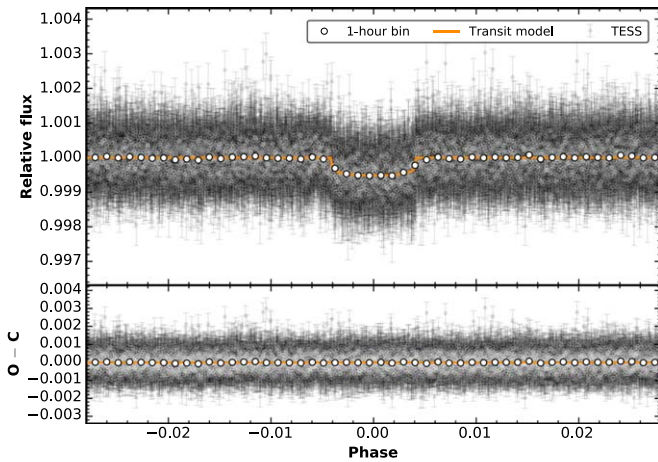
Figure 4. Top: phase-folded TESS light curve of TOI-1751 b. The black points with error bars show the flattened PDCSAP flux from 13 transits, where the error bars are calculated by adding the jitter and instrument uncertainty in quadrature. The orange line shows the best-fit (median) transit model from the joint RV and transit analysis. For clarity, the data are also shown in 1 hr bins (white circles). Bottom: residual flux between the best-fit (median) transit model and the data.

(Rowe et al. 2014), K2-199 c (Mayo et al. 2018), and Kepler-276 c and d (Xie 2014). The analyses of these other sub-Neptunes are hindered by degeneracies between volatile-rich and rocky interiors, which are also present for TOI-1751 b.

Although TOI-1751 is likely a thin-disk star, metal-poor Neptune-hosting stars are typically enriched in alpha elements (Adibekyan et al. 2012). This suggests that planets orbiting these stars had fewer metals and more water available when forming. We thus favor a volatile-rich interior composition for TOI-1751 b (see Section 5.2).

5.2. Interior Composition

The number of exoplanets with radii greater than $\sim 3 R_\oplus$ declines sharply, with planets between 2.7 and 3.0 $R_\oplus$ around FGK stars within 100 days being up to 10 times more common than planets between 3.3 and 3.7 $R_\oplus$ (Fulton & Petigura 2018; Hsu et al. 2019). Currently, the only proposed mechanism for this phenomenon is the "fugacity crisis": the increased solubility of hydrogen in magma at high pressures (Kite et al. 2019). At $\sim 3 R_\oplus$, the pressures at the base of a planetary atmosphere are sufficient to sequester atmospheric hydrogen in magma. The associated loss of H_2 (and thus, volume) from the atmosphere during formation may thus decrease the occurrence of $\gtrsim 3 R_\oplus$ planets. This makes an interesting case for studying the interior composition of planets with a radius just below $\sim 3 R_\oplus$ such as TOI-1751 b. These planets may have sequestered hydrogen from their atmospheres, which may be observable as low atmospheric mass fractions.

The radius of TOI-1751 b ($2.77^{+0.15}_{-0.07} R_\oplus$) implies that it is unlikely to be a purely rocky planet (Rogers 2015). Furthermore, the installation ($\sim 75 S_\oplus$) and escape velocity (~ 25 km s^{-1}) of TOI-1751 b place it firmly on the right of the cosmic shoreline, implying that this planet has an atmosphere (Zahnle & Catling 2017).

However, mass and radius measurements alone are not sufficient to uniquely constrain planet composition (Adams et al. 2008; Rogers & Seager 2010). The planet's bulk density is consistent with both a rocky interior with a few percent by mass H/He atmosphere and a volatile-rich interior with a H/He

atmosphere (see Figure 6). This degeneracy between silicate- and water-rich models is compounded by the unconstrained albedo and heat redistribution patterns, and is an ongoing challenge in characterizing sub-Neptunes (e.g., Valencia et al. 2013; Nixon & Madhusudhan 2021; Luque & Pallé 2022).

As shown in Figure 6, if TOI-1751 b has a rocky interior, it will have a higher H/He atmospheric mass fraction compared to if it has a volatile-rich interior. A volatile-rich planet has a lower bulk density than that of a planet with an iron-rich core, and thus needs a less massive atmosphere to make up the bulk density. The models described in Zeng et al. (2019) are also consistent with those described in Lopez & Fortney (2013), which predict a 0.5%–3% H/He atmosphere by mass for TOI-1751 b.

The relatively low atmospheric mass fraction of TOI-1751 b may have been sculpted by mass loss during evolution. Ongoing mass loss may be probed through future spectroscopic observations of Lyman α or metastable helium (e.g., Kulow et al. 2014; Spake et al. 2018), although the planet's long transit duration will make these observations resource intensive. Although this planet has a low Transmission Spectroscopy Metric (TSM = 20, Kempton et al. 2018), it may yet prove an interesting target for comparative atmospheric studies with next-generation instruments.

The mass, radius, and installation of TOI-1751 b are also consistent with models of putative irradiated ocean worlds (Aguichine et al. 2021). These models are composed of refractory layers (iron core and rocky mantle), a hydrosphere with an equation of state that extends to the plasma regime, and a steam atmosphere. Within this framework, TOI-1751 b is consistent with a $\sim 20\%$–50% water mass fraction for irradiation temperatures between 600 and 1000 K ($T_{\rm irr} = 700$ K for TOI-1751 b, see Equation (9) of Aguichine et al. 2021). The installation of TOI-1751 b at its current location also lies above the water vapor runaway greenhouse threshold (Zahnle & Catling 2017), suggesting that any water in this planet's atmosphere may exist as steam.

We used MAGRATHEA[40] (Huang et al. 2022) to investigate the composition of TOI-1751 b. MAGRATHEA is a 1D structure code that assumes fully differentiated planet layers: an iron core, a silicate mantle, a steam/water/ice hydrosphere, and a H/He atmosphere.

We note that these models do not encapsulate the true complexity of planet interiors, which may also include mixing between rock and water layers (Kovačević et al. 2022; Vazan et al. 2022). Ice and rock may remain mixed in planetary interiors for billions of years if no significant mass loss occurs. The timescale for a planet to lose its atmosphere via XUV-driven photoevaporation scales with M_p^2 (or, more precisely, $M_{\rm core}^2$) and scales inversely with installation (see Equation (4) in Lopez & Fortney 2013). A massive sub-Neptune-sized planet such as TOI-1751 b may have been able to resist photo-evaporative mass loss and thereby retain a small but non-negligible H/He atmosphere and, thus, an ice-rock mixture in its interior over its lifetime.

We used two MAGRATHEA modes to model TOI-1751 b: the default model and a composition solver, which we discuss in Sections 5.2.1 and 5.2.2, respectively.
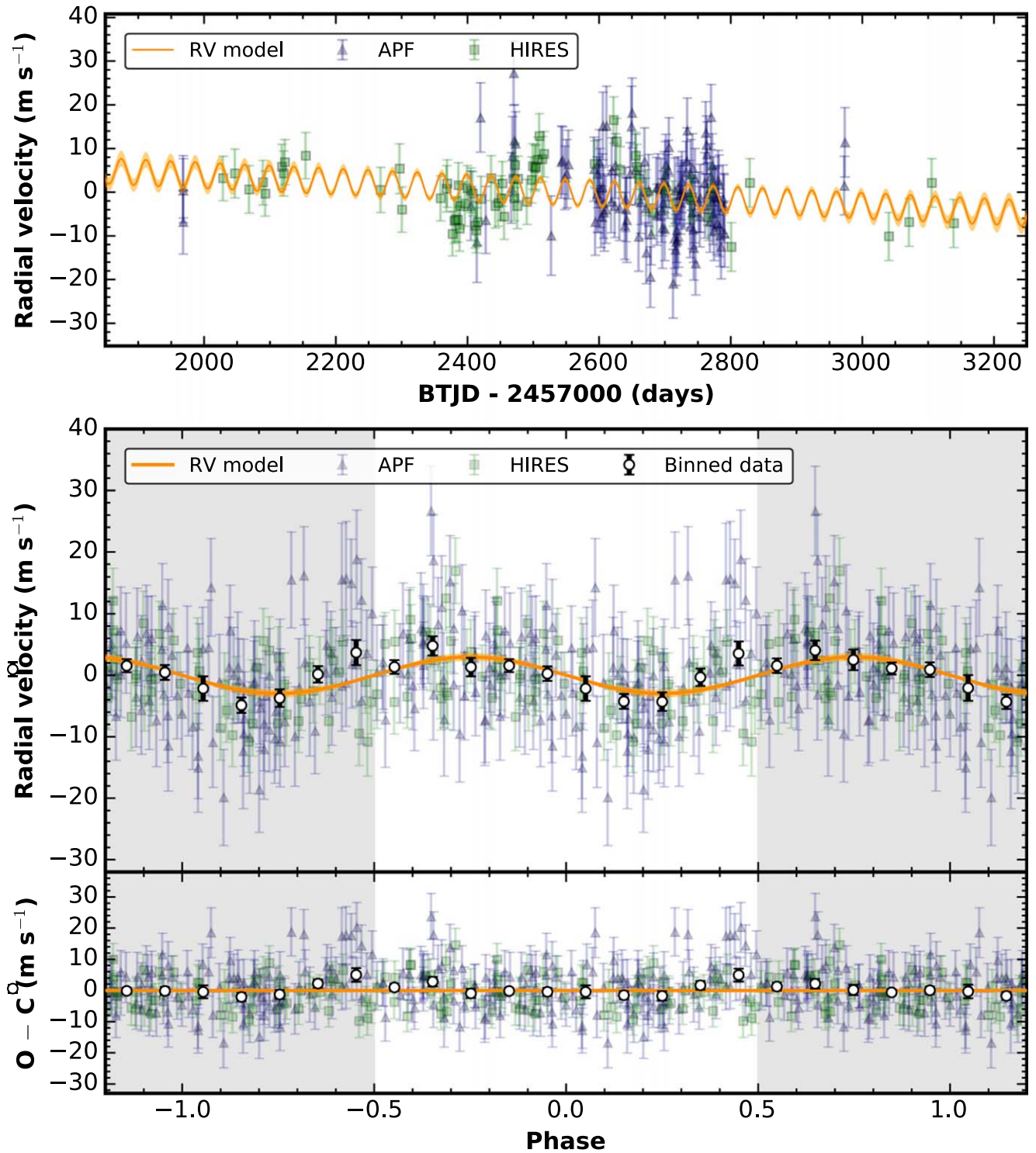
---

[40] https://github.com/Huang-CL/Magrathea

Figure 5. Top: RV measurements from APF (blue diamonds) and HIRES (green squares) and the best-fit (median) RV model (orange line) from the joint RV and transit analysis. For clarity, the RV offset for each instrument has been subtracted from the data, and the respective jitter terms have been combined with the instrumental uncertainties to produce the error bars. The orange-shaded region shows the 68% confidence range for the model. Middle: phase-folded radial velocities of TOI-1751 b, with the instrumental offsets and linear trend removed. The APF data (blue triangles) and HIRES data (green squares) are shown with error bars and the best-fit (median) RV model for the planet (orange line). The jitter term for each instrument has been added to the RV uncertainty in quadrature to calculate the error bars. The orange-shaded region indicates the model's 68% confidence range. For clarity, repeated orbital phase coverage is shown in the gray-shaded regions, and we have also binned the data to ~4 day intervals (white circles with error bars). Bottom: residual radial velocities between the best-fit (median) model and the data.

5.2.1. Solving for Planet Radius

Given the inherent degeneracies present in modeling sub-Neptune interiors, we consider several compositional "families" of solutions based on solar system objects and confirmed exoplanets in our analysis, differing in their core, mantle, water, and atmospheric mass fractions (CMF, MMF, WMF, and AMF, respectively). We summarize the families used in Table 3.
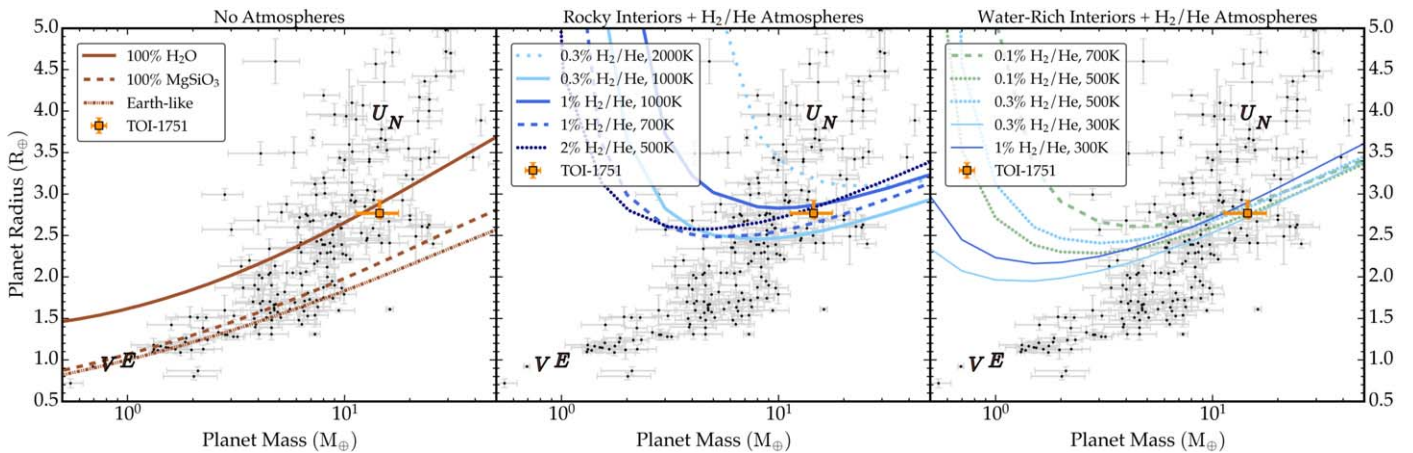
Figure 6. Mass vs. radius diagram showing confirmed planets with masses and radii measured to $>3\sigma$ precision (black points) and TOI-1751 b (orange). Each panel includes different theoretical composition curves from Zeng et al. (2019). Earth (E), Venus (V), Uranus (U), and Neptune (N) are also shown for context, with the precise masses and radii for these planets lying in the center of the letter symbol. TOI-1751 b is consistent with both rocky and water-rich models. Left: the Earth-like composition is assumed to be 32.5% Fe/Ni-metal plus 67.5% $MgSiO_3$-rock. Curves for 100% H_2O and 100% $MgSiO_3$ are also shown. Middle: composition curves assuming an Earth-like planet with the addition of an H_2/He atmosphere (made up of a mixture of 75% H_2 and 25% He). These curves are evaluated along interior adiabats at different internal specific entropies, labeled by the temperature of the corresponding specific entropy at 100 bar level in the gas envelope (2000 K is sparsely dashed, 1000 K is solid, 700 K is dashed, 500 K is dotted, 300 K is thin solid). Right: composition curves correspond to an Earth-like planet with an H/Heisothermal envelope at various surface temperatures atop an ice-VII (a cubic crystalline form of ice) layer.

Table 3
Compositional "Families" of Planet Interiors

Family	CMF	MMF	WMF	AMF	Reference	$R_p (R_\oplus)$
Earth-like	0.325	0.675	0	0	Seager et al. (2007)	1.97
Kepler-11c-like	0.18	0.49	0.33	0	Acuña et al. (2022)	2.67
Ganymede-like	0.065	0.485	0.45	0	Seager et al. (2007)	2.85
Neptune-like	0.125	0.125	0.62	0.13	Podolak et al. (1995)	4.99
Uranus-like	0.02	0.02	0.92	0.04	Podolak et al. (1995)	4.27
TOI-1751 b best fit	0.36	0.53	0.10	0.01	This work	2.77

Note. We used these inputs for the default MAGRATHEA mode to model TOI-1751 b in Section 5.2.1. For each model, we include the core mass fraction (CMF), mantle mass fraction (MMF), water mass fraction (WMF), and atmospheric mass fraction (AMF).

The default MAGRATHEA mode calculates the planet radius for a given planet mass and the distribution of mass between layers. For each step in enclosed mass, the pressure, density, and temperature are calculated, moving from $M = 0$ to $M = M_p$. This mode takes as input the temperature discontinuities at each boundary layer (if any), as well as the surface temperature. We assume thermal equilibrium between each boundary layer and a surface temperature equal to the calculated equilibrium temperature (820 K). We use the default phase diagrams and equations of state for the iron core and magnesium silicate mantle. We use an updated version of MAGRATHEA that includes tabulated equations of state for water in liquid, solid, vapor, and supercritical forms in the hydrosphere (Haldemann et al. 2020) and for a H/He atmosphere with solar composition (Chabrier & Debras 2021).

We find that Uranus-like, Neptune-like, and Earth-like compositions do not reproduce the measured radius of TOI-1751 b. We find that a WMF between that of a Kepler-11c-like and Ganymede-like model most closely reproduced the measured radius of TOI-1751 b, though these objects are very different in scale and environment.

We also manually refined the mass distribution between layers in order to optimize the model. In this, we set an atmospheric mass fraction of 1%, based on other models of planet composition (Lopez & Fortney 2013; Zeng et al. 2019). The model which most closely reproduces the radius of TOI-

1751 b includes a CMF of 36%, MMF of 53%, WMF of 10%, and an AMF of 1%. However, we stress that this is a possible composition rather than a prescriptive model of the interior of this planet.

5.2.2. Solving for Mass Fractions

The second MAGRATHEA input method used, a composition solver, calculates a planet's atmospheric and water mass fractions given a fixed planet mass and radius. Again, we assumed thermal equilibrium between each boundary layer and calculated the null albedo surface temperature to be 690 K. We drew 1000 samples from the planet mass and radius posteriors measured using RV and photometric data and used these as inputs for the composition solver. Our base model used an interior that has an Earth-like core-to-mantle ratio (32.5% core to 67.5% mantle). We then found the WMF (including a water vapor atmosphere) required to match the radius of TOI-1751 b. As shown in Figure 7, we found WMFs from 21% to 100% with a median WMF of 49%. This median WMF may suggest the planet formed beyond the snow line, much further out than its present location.

However, if we include an H/He atmosphere above supercritical water, the planet is consistent with a lower WMF. We now assumed an Earth-like core-to-mantle ratio and a WMF of 20%, set by the lowest WMF found in Section 4.2.1.
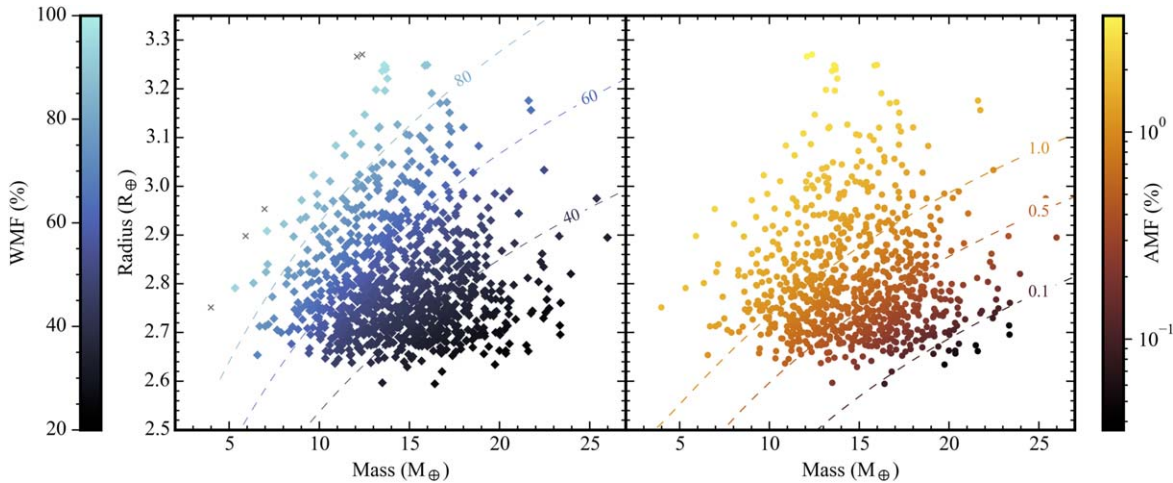
Figure 7. Mass vs. radius posterior samples from the joint transit and RV fit for TOI-1751 b modeled with MAGRATHEA. Left: models of TOI-1751 b assuming an Earth-like rock/iron ratio, no atmosphere (i.e., AMF = 0%), a supercritical and condensed water layer, and a water envelope. By allowing the planet's envelope to be made of water, the WMF required to reproduce the planet's radius is substantially reduced. Gray Xs mark mass and radius samples which are too low density to be modeled with AMF = 0%. Right: models of TOI-1751 b assuming an Earth-like mantle/core ratio, a WMF of 20%, and a non-ideal H/He atmosphere. The non-ideal atmosphere is less compressible than an ideal H/He envelope, and thus a smaller AMF is needed to reproduce the measured planet radius. Isocomposition curves for WMF and AMF are shown with dashed lines.

We then redistributed mass from the interior to form a H/He atmosphere. The atmosphere has an isothermal temperature profile with temperature increasing adiabatically at pressures above 100 bar (similar to the models of Nixon & Madhusudhan 2021). The AMF under this model ranges from 0.04% to 3.65% with a median of 0.72% (see Figure 7), much smaller than the atmospheric mass fractions of Neptune and Uranus. These findings are consistent with Section 5.2.1 and demonstrate the range of possible interior solutions for TOI-1751 b.

6. Conclusions

In this work, we study the solar-type star TOI-1751 using TESS photometry, and Keck/HIRES and APF/Levy RV observations. We confirm the planetary nature of TOI-1751 b, a transiting sub-Neptune, and measure its radius ($2.77^{+0.15}_{-0.07} R_\oplus$) and mass ($14.5^{+3.15}_{-3.14} M_\oplus$). From these measurements, we infer a bulk density of $3.6 \pm 0.9 \, \mathrm{g \, cm^{-3}}$. This points to several possible compositions: a rocky planet with a H/He atmosphere, a sub-Neptune with a volatile-rich interior, or an irradiated ocean planet with a volatile-rich interior and steam atmosphere.

TOI-1751 is a metal-poor ([Fe/H] = -0.40 ± 0.06) star, and as such, may have had a water-enriched protoplanetary disk (Adibekyan et al. 2012). We thus favor a volatile-rich (i.e., metal-poor) interior for this planet. We find its bulk density ($3.6 \pm 0.9 \, \mathrm{g \, cm^{-3}}$) can be matched by a volatile-rich interior with an atmosphere mass fraction of ~1%. TOI-1751 b is a relatively long period (37.47 days) but highly irradiated ($T_\mathrm{eq} = 820$ K) planet, giving us an insight into the small warm Neptune population with precisely measured masses and radii.

Acknowledgments

Appendix

In this Appendix, we present the RV observations used in our analysis (Table 4), as well as corner plots from the joint photometry and RV analysis (Figures 8, 9).

Table 4
TOI-1751 RV and S Value

Time (BJD-2457000)	RV (m s^{-1})	RV Error (m s^{-1})	S Value	S Value Error Error	Telescope/Instrument
1967.950094	5.017768	5.730939	0.122338	0.002	APF/Levy
1967.964422	−4.575683	5.527218	0.134032	0.002	APF/Levy
1967.978948	−2.429906	5.696315	0.133791	0.002	APF/Levy
2028.820286	2.559080	1.589164	0.121900	0.001	Keck/HIRES
2046.821867	3.707988	2.554524	0.123700	0.001	Keck/HIRES
…	…	…	…	…	…
2972.084400	5.696147	4.716573	0.130909	0.002	APF/Levy
2972.912956	5.916581	6.856952	0.122151	0.002	APF/Levy
3040.082792	−10.693290	2.534608	0.139400	0.001	Keck/HIRES
3070.930568	−7.465276	2.530681	0.140700	0.001	Keck/HIRES
3104.798844	1.547328	2.637302	0.140500	0.001	Keck/HIRES
3138.958952	−7.741875	2.594161	0.140500	0.001	Keck/HIRES

(This table is available in its entirety in machine-readable form.)
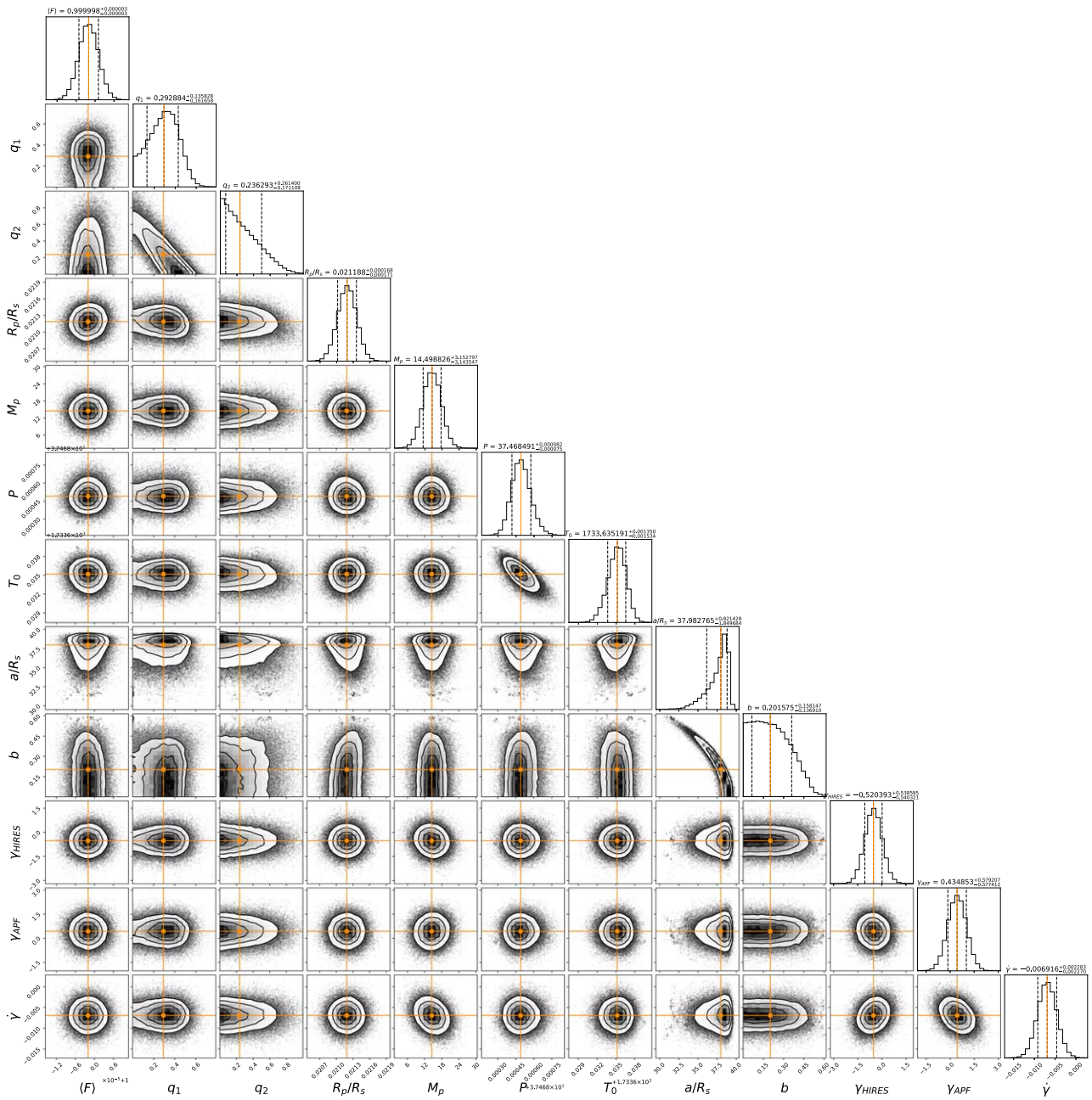
Figure 8. Posterior probability distributions for the joint RV and transit fit parameters for TOI-1751 b. The orange lines indicate the median value of the sample distribution, and the dashed black lines indicate a 68% interquantile range.
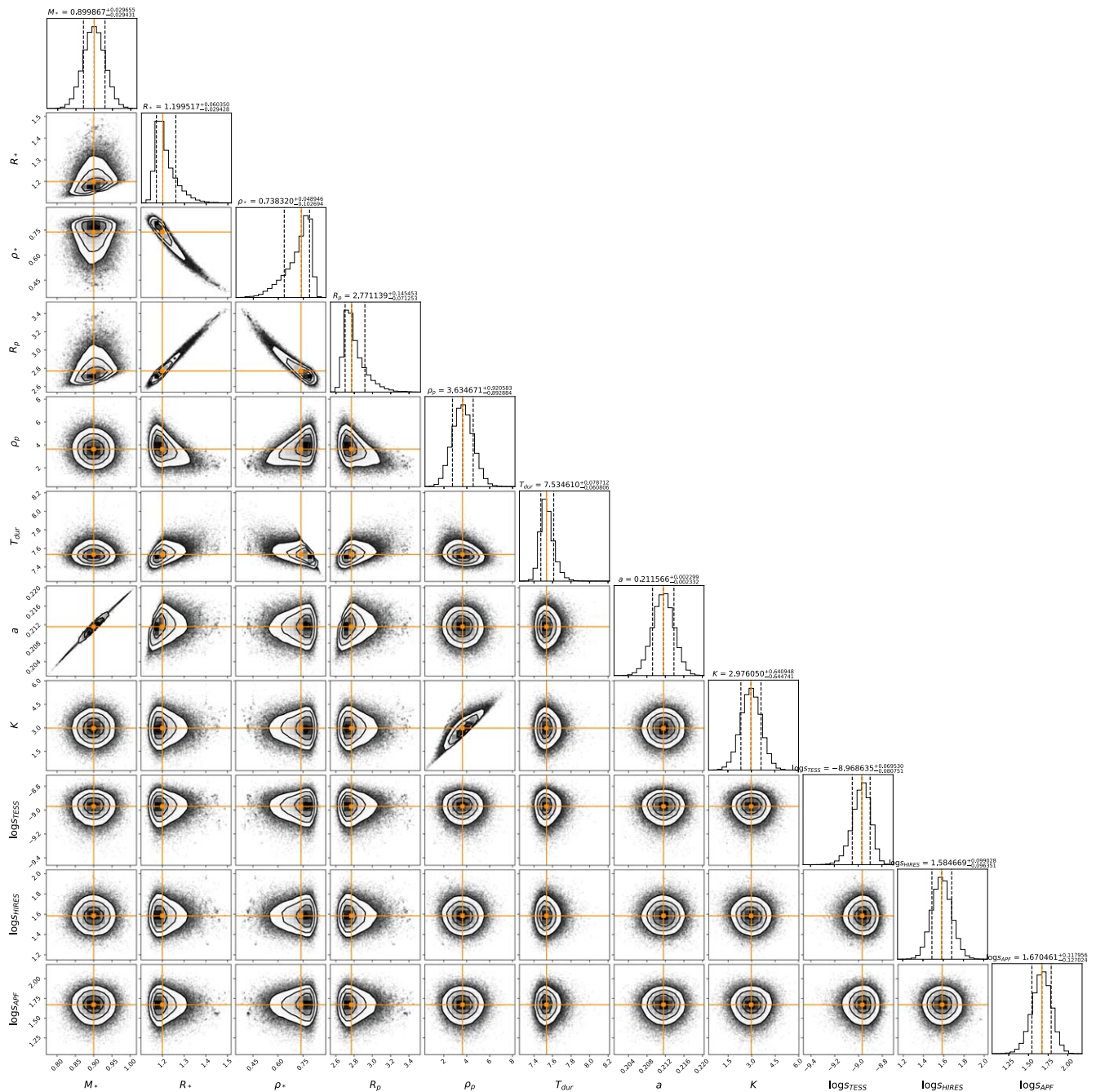
Figure 9. Auxiliary posterior distributions for the joint RV and transit fit parameters for TOI-1751 b. The orange lines indicate the median value of the sample distribution, and the dashed black lines indicate a 68% interquantile range.

ORCID iDs

Anmol Desai ⊙ https://orcid.org/0009-0000-9206-5589
Emma V. Turtelboom ⊙ https://orcid.org/0000-0002-1845-2617
Caleb K. Harada ⊙ https://orcid.org/0000-0001-5737-1687
Courtney D. Dressing ⊙ https://orcid.org/0000-0001-8189-0233
David R. Rice ⊙ https://orcid.org/0000-0001-6009-8685
Joseph M. Akana Murphy ⊙ https://orcid.org/0000-0001-8898-8284
Casey L. Brinkman ⊙ https://orcid.org/0000-0002-4480-310X
Ashley Chontos ⊙ https://orcid.org/0000-0003-1125-2564
Fei Dai ⊙ https://orcid.org/0000-0002-8958-0683

Michelle L. Hill ⊙ https://orcid.org/0000-0002-0139-4756
Tara Fetherolf ⊙ https://orcid.org/0000-0002-3551-279X
Steven Giacalone ⊙ https://orcid.org/0000-0002-8965-3969
Andrew W. Howard ⊙ https://orcid.org/0000-0001-8638-0320
Daniel Huber ⊙ https://orcid.org/0000-0001-8832-4488
Howard Isaacson ⊙ https://orcid.org/0000-0002-0531-1073
Stephen R. Kane ⊙ https://orcid.org/0000-0002-7084-0529
Jack Lubin ⊙ https://orcid.org/0000-0001-8342-7736
Mason G. MacDougall ⊙ https://orcid.org/0000-0003-2562-9043
Andrew W. Mayo ⊙ https://orcid.org/0000-0002-7216-2135
Teo Močnik ⊙ https://orcid.org/0000-0003-4603-556X

Alex S. Polanski ⬡ https://orcid.org/0000-0001-7047-8681
Malena Rice ⬡ https://orcid.org/0000-0002-7670-670X
Paul Robertson ⬡ https://orcid.org/0000-0003-0149-9678
Ryan A. Rubenzahl ⬡ https://orcid.org/0000-0003-3856-3143
Judah Van Zandt ⬡ https://orcid.org/0000-0002-4290-6826
Lauren M. Weiss ⬡ https://orcid.org/0000-0002-3725-3058
Allyson Bieryla ⬡ https://orcid.org/0000-0001-6637-5401
Lars A. Buchhave ⬡ https://orcid.org/0000-0003-1605-5666
Jon M. Jenkins ⬡ https://orcid.org/0000-0002-4715-9460
Veselin B. Kostov ⬡ https://orcid.org/0000-0001-9786-1031
Alan M. Levine ⬡ https://orcid.org/0000-0001-8172-0453
Jorge Lillo-Box ⬡ https://orcid.org/0000-0003-3742-1987
M. Paegert ⬡ https://orcid.org/0000-0001-8120-7457
Markus Rabus ⬡ https://orcid.org/0000-0003-2935-7196
S. Seager ⬡ https://orcid.org/0000-0002-6892-6948
Keivan G. Stassun ⬡ https://orcid.org/0000-0002-3481-9052
Eric B. Ting ⬡ https://orcid.org/0000-0002-8219-9505
David Watanabe ⬡ https://orcid.org/0000-0002-3555-8464
Joshua N. Winn ⬡ https://orcid.org/0000-0002-4265-047X

References

Acuña, L., Lopez, T. A., Morel, T., et al. 2022, A&A, 660, A102
Adams, E. R., Seager, S., & Elkins-Tanton, L. 2008, ApJ, 673, 1160
Adibekyan, V. Z., Santos, N. C., Sousa, S. G., et al. 2012, A&A, 543, A89
Agol, E., Luger, R., & Foreman-Mackey, D. 2020, AJ, 159, 123
Aguichine, A., Mousis, O., Deleuil, M., & Marcq, E. 2021, ApJ, 914, 84
Armstrong, D. J., Osborn, A., Adibekyan, V., et al. 2023, MNRAS, 524, 5804
Astropy Collaboration, Price-Whelan, A. M., Lim, P. L., et al. 2022, ApJ, 935, 167
Astropy Collaboration, Price-Whelan, A. M., Sipőcz, B. M., et al. 2018, AJ, 156, 123
Astropy Collaboration, Robitaille, T. P., Tollerud, E. J., et al. 2013, A&A, 558, A33
Bensby, T. 2004, PhD thesis, University of Lund, Sweden
Bensby, T., & Feltzing, S. 2010, in IAU Symp. 265, Chemical Abundances in the Universe: Connecting First Stars to Planets, ed. K. Cunha, M. Spite, & B. Barbuy (Cambridge: Cambridge Univ. Press), 300
Bitsch, B., Raymond, S. N., & Izidoro, A. 2019, A&A, 624, A109
Brandt, G. M., Brandt, T. D., & McCully, C. 2020, AJ, 160, 25
Brasseur, C. E., Phillip, C., Fleming, S. W., Mullally, S. E., & White, R. L., 2019 Astrocut: Tools for creating cutouts of TESS images, Astrophysics Source Code Library, record, ascl:1905.007
Buchhave, L. A., Latham, D., Johansen, A., et al. 2012, Natur, 486, 375
Butler, R. P., Marcy, G. W., Williams, E., et al. 1996, PASP, 108, 500
Campante, T. L., Barclay, T., Swift, J. J., et al. 2015, ApJ, 799, 170
Cannon, A. J., & Pickering, E. C. 1921, AnHar, 96, 1
Canto Martins, B. L., Gomes, R. L., Messias, Y. S., et al. 2020, ApJS, 250, 20
Carrillo, A., Hawkins, K., Bowler, B. P., Cochran, W., & Vanderburg, A. 2020, MNRAS, 491, 4365
Chabrier, G., & Debras, F. 2021, ApJ, 917, 4
Chiang, E., & Laughlin, G. 2013, MNRAS, 431, 3444
Chontos, A., Akana Murphy, J. M., MacDougall, M. G., et al. 2022, AJ, 163, 297
Ciardi, D. R., Beichman, C. A., Horch, E. P., & Howell, S. B. 2015, ApJ, 805, 16
Coelho, P., Barbuy, B., Meléndez, J., Schiavon, R. P., & Castilho, B. V. 2005, A&A, 443, 735
Dattilo, A., Batalha, N. M., & Bryson, S. 2023, AJ, 166, 122
Fetherolf, T., Pepper, J., Simpson, E., et al. 2023, ApJS, 268, 4
Főrész, G. 2008, PhD thesis, University of Szeged, Hungary
Foreman-Mackey, D. 2016, JOSS, 1, 24
Foreman-Mackey, D., Luger, R., Agol, E., et al. 2021, JOSS, 6, 3285
Foreman-Mackey, D., Savel, A., Luger, R., et al. 2021, exoplanet-dev/exoplanet v0.5.1, Zenodo, doi:10.5281/zenodo.1998447
Fulton, B. J., & Petigura, E. A. 2018, AJ, 156, 264
Fulton, B. J., Petigura, E. A., Blunt, S., & Sinukoff, E. 2018, PASP, 130, 044504
Fulton, B. J., Petigura, E. A., Howard, A. W., et al. 2017, AJ, 154, 109
Furlan, E., Ciardi, D. R., Everett, M. E., et al. 2017, AJ, 153, 71
Gagné, J., Mamajek, E. E., Malo, L., et al. 2018, ApJ, 856, 23
Gaia Collaboration, Vallenari, A., Brown, A. G. A., et al. 2023, A&A, 674, A1

Gavel, D., Kupke, R., Dillon, D., et al. 2014, Proc. SPIE, 9148, 914805
Georgieva, I. Y., Persson, C. M., Barragán, O., et al. 2021, MNRAS, 505, 4684
Ginsburg, A., Sipőcz, B. M., Brasseur, C. E., et al. 2019, AJ, 157, 98
Ginzburg, S., Schlichting, H. E., & Sari, R. 2018, MNRAS, 476, 759
Guerrero, N. M., Seager, S., Huang, C. X., et al. 2021, ApJS, 254, 39
Haldemann, J., Alibert, Y., Mordasini, C., & Benz, W. 2020, A&A, 643, A105
Harris, C. R., Millman, K. J., van der Walt, S. J., et al. 2020, Natur, 585, 357
Hirsch, L. A., Ciardi, D. R., Howard, A. W., et al. 2019, ApJ, 878, 50
Hoffman, M. D., & Gelman, A. 2011, JMLR, 15, 1593
Høg, E., Fabricius, C., Makarov, V. V., et al. 2000, A&A, 355, L27
Hormuth, F., Brandner, W., Hippler, S., & Henning, T. 2008, JPhCS, 131, 012051
Howard, A. W., Johnson, J. A., Marcy, G. W., et al. 2010, ApJ, 721, 1467
Howell, S. B., Everett, M. E., Sherry, W., Horch, E., & Ciardi, D. R. 2011, AJ, 142, 19
Hsu, D. C., Ford, E. B., Ragozzine, D., & Ashby, K. 2019, AJ, 158, 109
Huang, C., Rice, D. R., & Steffen, J. H. 2022, MNRAS, 513, 5256
Huang, C. X., Vanderburg, A., Pál, A., et al. 2020a, RNAAS, 4, 204
Huang, C. X., Vanderburg, A., Pál, A., et al. 2020b, RNAAS, 4, 206
Hunter, J. D. 2007, CSE, 9, 90
Husser, T. O., Wende-von Berg, S., Dreizler, S., et al. 2013, A&A, 553, A6
Izidoro, A., Schlichting, H. E., Isella, A., et al. 2022, ApJL, 939, L19
Jenkins, J. M. 2002, ApJ, 575, 493
Jenkins, J. M., Chandrasekaran, H., McCauliff, S. D., et al. 2010, Proc. SPIE, 7740, 77400D
Jenkins, J. M., Tenenbaum, P., Seader, S., et al. 2020, Kepler Science Document KSCI-19081-003
Jenkins, J. M., Twicken, J. D., McCauliff, S., et al. 2016, Proc. SPIE, 9913, 99133E
Kass, R. E., & Raftery, A. E. 1995, JASA, 90, 773
Kempton, E. M. R., Bean, J. L., Louie, D. R., et al. 2018, PASP, 130, 114401
Kipping, D. M. 2013, MNRAS, 435, 2152
Kite, E. S., Fegley, B., Jr., Schaefer, L., & Ford, E. B. 2019, ApJL, 887, L33
Kovács, G., Zucker, S., & Mazeh, T. 2002, A&A, 391, 369
Kovačević, T., González-Cataldo, F., Stewart, S. T., & Militzer, B. 2022, NatSR, 12, 13055
Kulow, J. R., France, K., Linsky, J., & Loyd, R. O. P. 2014, ApJ, 786, 132
Kumar, R., Carroll, C., Hartikainen, A., & Martin, O. A. 2019, JOSS, 4, 1143
Kupke, R., Gavel, D., Roskosi, C., et al. 2012, Proc. SPIE, 8447, 84473G
Kurucz, R. L. 1992, in IAU Symp. 149, The Stellar Populations of Galaxies, ed. R. L. Galaxies (Dordrecht: Kluwer), 225
Lacedelli, G., Malavolta, L., Borsato, L., et al. 2021, MNRAS, 501, 4148
Lee, E. J., & Chiang, E. 2016, ApJ, 817, 90
Lee, E. J., Karalis, A., & Thorngren, D. P. 2022, ApJ, 941, 186
Léger, A., Selsis, F., Sotin, C., et al. 2004, Icar, 169, 499
Lester, K. V., Matson, R. A., Howell, S. B., et al. 2021, AJ, 162, 75
Li, J., Tenenbaum, P., Twicken, J. D., et al. 2019, PASP, 131, 024506
Lightkurve Collaboration, Cardoso, J. V. D. M., Hedges, C., et al. 2018, Lightkurve: Kepler and TESS time series analysis in Python, Astrophysics Source Code Library, ascl:1812.013
Lillo-Box, J., Barrado, D., & Bouy, H. 2012, A&A, 546, A10
Lillo-Box, J., Barrado, D., & Bouy, H. 2014, A&A, 566, A103
Lindgren, L. 2018, Technical Report GAIA-C3-TN-LU-LL-124-01, Lund Observatory
Loebman, S. R., Roškar, R., Debattista, V. P., et al. 2011, ApJ, 737, 8
Lomb, N. R. 1976, Ap&SS, 39, 447
Lopez, E. D., & Fortney, J. J. 2013, ApJ, 776, 2
Luque, R., & Pallé, E. 2022, Sci, 377, 1211
MacDougall, M. G., Petigura, E. A., Gilbert, G. J., et al. 2023, AJ, 166, 33
Mamajek, E. E., & Hillenbrand, L. A. 2008, ApJ, 687, 1264
Martin, D. C., Fanson, J., Schiminovich, D., et al. 2005, ApJL, 619, L1
MAST Team 2021, TESS Light Curves—All Sectors, STScI/MAST
Mayo, A. W., Vanderburg, A., Latham, D. W., et al. 2018, AJ, 155, 136
Miguel, Y., & Vazan, A. 2023, RemS, 15, 681
Neuenschwander, B. A., & Helled, R. 2022, MNRAS, 512, 3124
Nissen, P. E. 2004, in Origin and Evolution of the Elements, ed. A. McWilliam & M. Rauch (Cambridge: Cambridge Univ. Press), 154
Nixon, M. C., & Madhusudhan, N. 2021, MNRAS, 505, 3414
Owen, J. E., & Wu, Y. 2013, ApJ, 775, 105
Paegert, M., Stassun, K. G., Collins, K. A., et al. 2022, yCat, IV/39
pandas development team 2020, pandas-dev/pandas: Pandas, v2.2.1, Zenodo, doi:10.5281/zenodo.10537285
Petigura, E. A., Howard, A. W., Marcy, G. W., et al. 2017, AJ, 154, 107
Podolak, M., & Helled, R. 2012, ApJL, 759, L32
Podolak, M., Weizman, A., & Marley, M. 1995, P&SS, 43, 1517
Quinn, P. J., Hernquist, L., & Fullagar, D. P. 1993, ApJ, 403, 74

Radovan, M. V., Lanclos, K., Holden, B. P., et al. 2014, Proc. SPIE, 9145, 91452B

Ricker, G. R., Winn, J. N., Vanderspek, R., et al. 2014, Proc. SPIE, 9143, 914320

Rodriguez, D. 2016, dr-rodriguez/Kinematics-App: Stellar Kinematics v1.0, 0 Zenodo, doi:10.5281/zenodo.192159

Rogers, J. G., Gupta, A., Owen, J. E., & Schlichting, H. E. 2021, MNRAS, 508, 5886

Rogers, L. A. 2015, ApJ, 801, 41

Rogers, L. A., & Seager, S. 2010, ApJ, 712, 974

Rowe, J. F., Bryson, S. T., Marcy, G. W., et al. 2014, ApJ, 784, 45

Salvatier, J., Wiecki, T. V., & Fonnesbeck, C. 2016, PeerJ Comp. Sci., 2, e55

Savel, A. B., Dressing, C. D., Hirsch, L. A., et al. 2020, AJ, 160, 287

Scargle, J. D. 1982, ApJ, 263, 835

Schlegel, D. J., Finkbeiner, D. P., & Davis, M. 1998, ApJ, 500, 525

Schönrich, R., & Binney, J. 2009, MNRAS, 399, 1145

Scott, N. J., Howell, S. B., Gnilka, C. L., et al. 2021, FrASS, 8, 138

Seager, S., Kuchner, M., Hier-Majumder, C. A., & Militzer, B. 2007, ApJ, 669, 1279

Siverd, R. J., Brown, T. M., Barnes, S., et al. 2018, Proc. SPIE, 10702, 107026C

Skrutskie, M. F., Cutri, R. M., Stiening, R., et al. 2006, AJ, 131, 1163

Smith, J. C., Stumpe, M. C., Van Cleve, J. E., et al. 2012, PASP, 124, 1000

Spake, J. J., Sing, D. K., Evans, T. M., et al. 2018, Natur, 557, 68

Stassun, K. G., Collins, K. A., & Gaudi, B. S. 2017, AJ, 153, 136

Stassun, K. G., Corsaro, E., Pepper, J. A., & Gaudi, B. S. 2018, AJ, 155, 22

Stassun, K. G., & Torres, G. 2016, AJ, 152, 180

Steffen, J. H., Fabrycky, D. C., Agol, E., et al. 2013, MNRAS, 428, 1077

Strehl, K. 1902, AN, 158, 89

Stumpe, M. C., Smith, J. C., Catanzarite, J. H., et al. 2014, PASP, 126, 100

Stumpe, M. C., Smith, J. C., Van Cleve, J. E., et al. 2012, PASP, 124, 985

Theano Development Team 2016, arXiv:1605.02688

Torres, G., Andersen, J., & Giménez, A. 2010, A&ARv, 18, 67

Twicken, J. D., Catanzarite, J. H., Clarke, B. D., et al. 2018, PASP, 130, 064502

Valencia, D., Guillot, T., Parmentier, V., & Freedman, R. S. 2013, ApJ, 775, 10

van der Kruit, P. C., & Freeman, K. C. 2011, ARA&A, 49, 301

Van der Velden, E. 2020, JOSS, 5, 2004

Van Zandt, J., Petigura, E. A., MacDougall, M., et al. 2023, AJ, 165, 60

Vazan, A., Sari, R., & Kessel, R. 2022, ApJ, 926, 150

Venturini, J., Guilera, O. M., Haldemann, J., Ronco, M. P., & Mordasini, C. 2020, A&A, 643, L1

Venturini, J., & Helled, R. 2017, ApJ, 848, 95

Vogt, S. S., Radovan, M., Kibrick, R., et al. 2014, PASP, 126, 359

Wright, E. L., Eisenhardt, P. R. M., Mainzer, A. K., et al. 2010, AJ, 140, 1868

Wyatt, M. C., Kral, Q., & Sinclair, C. A. 2020, MNRAS, 491, 782

Xie, J.-W. 2014, ApJS, 210, 25

Yee, S. W., Petigura, E. A., & von Braun, K. 2017, ApJ, 836, 77

Zahnle, K. J., & Catling, D. C. 2017, ApJ, 843, 122

Zeng, L., Jacobsen, S. B., Sasselov, D. D., et al. 2019, PNAS, 116, 9723

Zhu, W., & Wu, Y. 2018, AJ, 156, 92